Microwave Spectroscopic and Computational Study of Prototypical Isocyanates and Isothiocyanates

By

Joseph Stitsky

A thesis submitted to the Faculty of Graduate Studies of the University of Manitoba in partial fulfillment of the requirements of the degree of

Master of Science

Department of Chemistry

University of Manitoba

Winnipeg, Canada

Copyright © 2020 by Joseph Stitsky

Abstract

This thesis outlines the microwave spectroscopic and computational study of prototypical isocyanates (RNCO) and isothiocyanates (RNCS) to better understand how the geometry around nitrogen is influenced by different side chains (R) and terminal chalcogen substitution. Specifically, this thesis describes the comprehensive research done on allyl isothiocyanate ($H_2C{=}CHCH_2$-NCS) (for a comparison with previous results for allyl isocyanate ($H_2C{=}CHCH_2$-NCO)) along with a study of benzyl isocyanate ($C_6H_5CH_2$-NCO) which was compared to a set of theoretical predictions for benzyl isothiocyanate ($C_6H_5CH_2$-NCS). Microwave spectroscopy is a useful technique for these investigations as the data collected using the broadband chirped-pulse Fourier transform microwave (cp-FTMW) and the narrowband Balle-Flygare Fourier transform microwave (FTMW) spectrometers are intrinsically sensitive to the underlying molecular geometries of the conformers in each sample.

In the allyl-NCS study, microwave transitions were assigned to two conformers including the first report of the lowest energy form and its heavy atom minor isotopologues which enabled a structural derivation. A comparison of the calculated nitrogen hybridization between allyl-NCS and allyl-NCO revealed a change from a ~ $sp^{1.5}$ environment in allyl-NCO to a ~ sp environment in allyl-NCS which is consistent with the change in the experimentally derived CNC bond angles. For benzyl-NCO, transitions were assigned to the global minimum conformer and its ^{13}C isotopologues. An analysis of the nitrogen hybridization revealed that the benzyl-NCO nitrogen electronic environment is most similar to that of its allyl counterpart and a similar result was confirmed based on the computational predictions for benzyl-NCS when compared with allyl-NCS. A comparison of the results of this thesis with studies of other RNCO and RNCS species in

the literature highlights the subtle balance of effects that the R group and terminal chalcogen substitution have on the properties of isocyanates and isothiocyanates.

Acknowledgements

First, I would like to express my deepest gratitude to my M.Sc. supervisor Dr. Jennifer van Wijngaarden for her patience and guidance over the past two years. Through our discussions over the course of my program, I've greatly improved my research, writing and critical thinking abilities which would not have been possible without her input.

Additionally, I would like to thank my committee members Dr. Gregg Tomy and Dr. Feiyue Wang for their advice over the course of my M.Sc. program.

I would also like to express my gratitude to current and past van Wijngaarden group members Weslley G.D.P. Silva and Dr. Wenhao Sun, respectively for our discussions and collaborations particularly at the beginning of my program while I was learning many new things in a relatively short period of time.

Additional gratitude also goes to current and past van Wijngaarden group members Katrina Bergmann, Paul Sogeke, Carolyn Gregory and Tamanna Poonia for all of their input and support.

Lastly, I would also like to thank my parents Virginia and Michael Stitsky for all their feedback and support over the years.

Table of Contents

Abstract…….I

Acknowledgements……III

Table of Contents……...IV

List of Figures……...VII

List of Tables...…….....XII

Contributions of Authors…….XIV

Chapter 1. Introduction…….1

1.1 Chemistry of the Interstellar Medium…….1

1.2 Structural Changes due to Substitution……...1

1.3 Conformational Space and Microwave Spectroscopy……...…….5

1.4 Moments of Inertia…….6

1.5 Rotational Constants and Transition Frequency Equations……7

1.6 Selection Rules...……9

1.7 Centrifugal Distortion……...12

1.8 ^{14}N Quadrupole Hyperfine Splitting…….13

References……..16

Chapter 2. Experimental and Computational Methods……...19

2.1 Computational Methods……...19

2.2 Sample Preparation and Supersonic Jet Expansion……...21

2.3 Chirped Pulse FTMW Spectrometer…….22

2.4 Balle-Flygare FTMW Spectrometer…….24

2.5 Spectral and Structural Analysis……...28

2.6 General Microwave Study Timeline…….30

References……..33

Chapter 3. Microwave Spectroscopic and Computational Study of Allyl-NCS…….....36

3.1 Abstract……....36

3.2 Introduction..……37

3.3 Experimental Methods…….40

3.4 Computational Methods...……42

3.5 Spectral Analysis.…….46

3.6 Discussion……50

3.7 Conclusion...…….56

References……..58

Chapter 4. Microwave Spectroscopy of benzyl-NCO with associated benzyl-NCO and benzyl-NCS computational analyses……..64

4.1 Introduction....……..64

4.2 Computational Details……..65

4.3 Experimental Details.....……67

4.4 Spectral Analysis……..67

4.5 Structural Determination……..73

4.6 Discussion……74

References……..85

Chapter 5. Conclusions and Future Work……...88

References.....92

List of Figures

Fig 1.1 Chemical structure of a) HCCNCO and b) HCCNCS with the value of the CNC angle for both molecules included……..……..2

Fig. 1.2 Chemical structure of a) phenyl-NCO and b) phenyl-NCS highlighting the experimentally derived CNC angle for both molecules…….....3

Fig. 1.3 Connectivity diagram of allyl-NCS in which all carbon atoms are numbered and the dihedral angles δ (C_1-C_2-C_3-N) and θ (C_2-C_3-N-C_4) are labelled. Both dihedrals have a value of 180°……..4

Fig. 1.4 Connectivity diagram of a) benzyl-NCO and b) benzyl-NCS in which all carbon atoms are numbered and the dihedral angles δ (C_5-C_4-C_7-N) and θ (C_4-C_7-N-C_8) are labelled. In this figure, both dihedrals have values of 180°……....5

Fig. 1.5 Energy level diagram for a linear rotor showing the rotational transitions and the corresponding frequency values. The spacing between energy levels in this diagram is not to scale.……...10

Fig. 1.6 Asymmetric rotor energy level diagram (middle) correlated to the prolate (left) and oblate (right) symmetric top limits. In this diagram, the spacings between rotational energy levels is not to scale..…….....11

Fig. 1.7 A section of the asymmetric rotor energy level diagram showing an example of a, b and c-type transitions between the J = 0 and the J = 1 rotational energy levels. The spacings between energy levels is not to scale.……....12

Fig. 1.8 Energy level diagram showing the hyperfine structure for the 2_{12} rotational energy level. The spacings between hyperfine components is not to scale…….....14

Fig. 2.1 An image of the 8-18 GHz cp-FTMW instrument in the van Wijngaarden lab...…….....22

Fig. 2.2 A schematic diagram showing the electronic circuit of the cp-FTMW instrument...…....23

Fig. 2.3 An image of the custom-built FTMW spectrometer in the van Wijngaarden lab.....25

Fig. 2.4 A schematic diagram showing the electronic circuit of the FTMW instrument.…...…....26

Fig. 3.1 Chemical structure of allyl-NCS showing dihedral angles δ (C_1-C_2-C_3-N) and θ (C_2-C_3-N-C_4). Both δ and θ are 180° in this image…...…….....38

Fig. 3.2 Sample 3 GHz segment of the cp-FTMW spectrum. The 5_{05}-4_{04} rotational transitions due to ^{13}C and ^{15}N species of conformer I are shown in the enhanced portion of the spectrum. (3 million FIDs)…….....41

Fig. 3.3 Sample Balle-Flygare FTMW spectrum (410 cycles) showing the 4_{13}-3_{12} rotational transition of conformer I including the ^{14}N hyperfine structure…….…….....42

Fig. 3.4 Three-dimensional potential energy surfaces of allyl-NCS obtained by scanning the dihedral angles δ and θ at the B3LYP, B3LYP-D3, B3LYP-D3(BJ) and MP2 methods with the cc-pVTZ basis set. The relative energies are plotted in units of kJ mol^{-1}……...…….....43

Fig. 3.5 Five optimized geometries corresponding to energy minima of allyl-NCS obtained at the B3LYP-D3(BJ)/cc-pVQZ level of theory. These geometries correspond to conformers Ia/Ib (δ = 0.9°/-0.9, θ = -43.2°/43.2°), II (δ = -0.3°, θ = 180.0°) and IIIa/IIIb (δ = -122.9°/122.9°, θ = -16.9°/16.9°). The Cartesian coordinates for all conformers are provided in Tables S1-S3 in the supporting information (SI) file…….....44

Fig. 3.6 a) Relaxation pathway calculated as a result of scanning the dihedral angle δ in 36 steps of 10º at the B3LYP/cc-pVQZ and B3LYP-D3(BJ)/cc-pVQZ levels of theory. b) Relaxation pathway calculated when scanning the dihedral angle θ in 36 steps of 10º, where the initial value of δ is 0º, at B3LYP/cc-pVQZ and B3LYP-D3(BJ)/cc-pVQZ levels of theory…….....46

Fig. 4.1 Optimized geometries of benzyl-NCO calculated at the APFD/aug-cc-pVTZ level of theory. In this figure, the numbering system for the carbon atoms is shown in the conformer I geometry. [a]Population distribution calculated using ZPE corrected electronic energies at 298.15 K……....68

Fig. 4.2 Structure of benzyl-NCO conformer I calculated at the APFD/aug-cc-pVTZ level showing the a, b and c principal inertial axes.....69

Fig. 4.3 A sample of the benzyl-NCO broadband spectrum from 8000 to 10 800 MHz showing transitions assigned to conformer I. An enhanced portion of the broadband spectrum showing the 6_{16}-5_{15} transition for different ^{13}C isotopologues is highlighted by a red rectangle.…….....70

Fig. 4.4 A 0.6 MHz segment of the benzyl-NCO FTMW spectrum showing the 10_{19}-9_{18} rotational transition for benzyl-NCO conformer I (820 cycles). In this figure, the assigned hyperfine structure due to the quadrupolar ^{14}N nucleus can be seen as well as the Doppler splitting caused by the introduction of the molecular beam parallel to the cavity axis.....71

Fig. 4.5 NCI analysis showing the intramolecular interactions of benzyl-NCO conformer I.....75

Fig. 4.6 Optimized geometry of the benzyl-NCO transition state for the interconversion of conformer I and conformer II as determined at the APFD/aug-cc-pVTZ level of theory……....77

Fig. 4.7 Energy profile for the interconversion of conformers I and II showing the ZPE corrected barrier for benzyl-NCO at 298.15 K. In this figure, the ZPE corrected energies were calculated at the APFD/aug-cc-pVTZ level of theory and the y-axis is not to scale…..…….....78

Fig. 4.8 Optimized geometries of benzyl-NCS conformers I and II calculated at the APFD/aug-cc-pVTZ level of theory. In this figure, the numbering system for the carbon atoms is shown in the conformer I geometry. [a]Population distribution calculated using ZPE corrected electronic energies at 298.15 K.....79

Fig. 4.9 Optimized geometry of the benzyl-NCS transition state for the interconversion of conformers I and II as determined at the APFD/aug-cc-pVTZ level of theory…….....80

Fig. 4.10 Energy profile for the interconversion of conformers I and II showing the ZPE corrected barrier for benzyl-NCS at 298.15 K. In this figure, the ZPE corrected energies were calculated at the APFD/aug-cc-pVTZ level of theory and the y-axis is not to scale…….....81

List of Tables

Table 3.1 Calculated Relative Energies, Relative Populations, Equilibrium Rotational Constants and Dipole Moment Components for the Conformers of Allyl Isothiocyanate……..……....45

Table 3.2 Ground State Spectroscopic Constants Obtained for the Parent, ^{34}S, ^{13}C and ^{15}N Species of Conformer I…….....48

Table 3.3 Ground State Spectroscopic Constants Obtained for the Parent and ^{34}S Species of Conformer III……....49

Table 3.4 Comparison of the Equilibrium (r_e) (B3LYP-D3(BJ)/cc-pVQZ)[a] and Effective Ground State (r_0) Geometries for Conformer I of Allyl-NCS and Allyl-NCO and Transition State Geometry (r_{ts}) for Ia/Ib Interconversion of Allyl-NCS (B3LYP-D3(BJ)/cc-pVQZ.….....50

Table 4.1 Rotational, centrifugal distortion and ^{14}N quadrupole coupling constants for the parent species and unique ^{13}C minor isotopologues of benzyl-NCO conformer I as well as those same parameters calculated at the APFD/aug-cc-pVTZ level…….72

Table 4.2 r_0 structure for benzyl-NCO conformer I along with the corresponding r_e structure calculated at the APFD/aug-cc-pVTZ level and the r_e structure of benzyl-NCS conformer I calculated at the same level of theory…….....73

Table 4.3 Comparison between experimentally derived spectroscopic constants and those determined at different levels of theory for benzyl-NCO conformer I…….....76

Contributions of Authors

1) The Conformers of Allyl-Isothiocyanate: A combined Microwave Spectroscopy and Computational Study[1]

Roles:

i) Joseph Stitsky – Collected and assigned experimental spectrum, performed calculations and prepared first draft of the manuscript as primary author.

ii) Weslley G.D.P. Silva – Assisted in assignment of experimental spectrum, performed calculations and edited manuscript.

iii) Wenhao Sun – Performed calculations and produced figures for manuscript

iv) Jennifer van Wijngaarden – Edited manuscript.

[1] A copy of this work has been published in the Journal of Physical Chemistry A under the citation: Stitsky, J.; Silva, W. G. D. P.; Sun, W.; van Wijngaarden, J. Conformers of Allyl-Isothiocyanate: A Combined Microwave Spectroscopy and Computational Study. *J. Phys. Chem. A.* **2020**, *124* (19), 3876-3885. Copyright © 2020 American Chemical Society.

Chapter 1. Introduction

1.1 Chemistry of the Interstellar Medium

The presence of various NCO and NCS containing molecules has been confirmed in the interstellar medium which is comprised of molecular gas clouds.[1] As an example, Snyder and Buhl detected emission lines in the ~ 88 GHz region that were attributed to isocyanic acid (H-NCO) based on previous laboratory measurements of its rotational spectrum.[2,3] Similarly, five rotational transitions were also observed by Frerking et al.[4] and assigned to isothiocyanic acid (H-NCS) using laboratory data.[3] This, in combination with the detection of other compounds such as H-OCN[5,6], H-SCN[7,8] and CH_3-NCO[9] proves the existence of various NCO and NCS-like species in interstellar space. Furthermore, because a rotational spectrum obtained and analyzed in a laboratory setting acts as a fingerprint when identifying species in astrophysical environments, this makes obtaining the laboratory assigned rotational spectrum crucial to understanding the chemistry of the interstellar medium.

1.2 Structural Changes due to Substitution

A comparison of these laboratory microwave studies has indicated a difference in geometry between a given isocyanate and the corresponding isothiocyanate. For example, a previous microwave study done by the van Wijngaarden group on ethynyl isothiocyanate (HCCNCS) determined that the most accurate fit of transitions in the rotational spectrum was obtained while assuming a linear molecule and this assignment was confirmed by the assignment of transitions due to ^{13}C and ^{34}S isotopologues in natural abundance.[10] In contrast, a microwave study of ethynyl isocyanate (HCCNCO) by Ross et al. produced an experimentally derived CNC bond angle of ~ 140.7° meaning that a ~ 40° change occurs as a result of terminal chalcogen substitution.[10,11] The

chemical structures of the two ethynyl molecules are shown in Fig. 1.1 where the CNC bond angles are highlighted.[10,11]

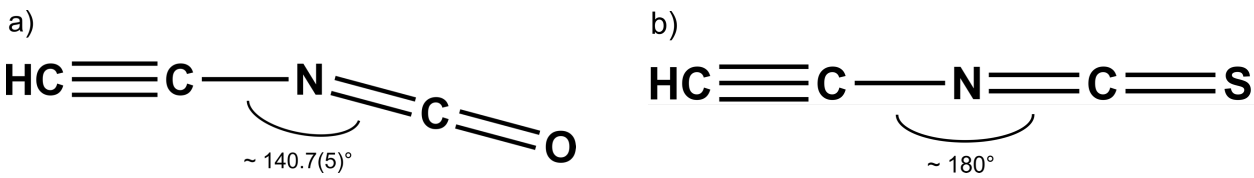

Fig 1.1 Chemical structure of a) HCCNCO and b) HCCNCS with the value of the CNC bond angle for both molecules included.

To further investigate this phenomenon, consider the microwave study done by the van Wijngaarden group on phenyl isocyanate (phenyl-NCO) and phenyl isothiocyanate (phenyl-NCS).[12] In this study, the microwave spectrum of both molecules was recorded from 4-26 GHz including transitions due to heavy atom isotopologues which allowed for a derivation of molecular structures.[12] The experimentally derived CNC bond angle for both phenyl molecules is shown in Fig. 1.2 and demonstrates that oxygen to sulfur substitution for the phenyl side chain leads to a ~ 10° increase in this angle which is ~ 30° smaller than the change that was observed for ethynyl group.[10–12] Furthermore, in the phenyl-NCO and phenyl-NCS study, a natural bond orbital (NBO) analysis was conducted on the optimized geometry of both molecules in order to calculate various electronic properties, most notably the hybridization state of the nitrogen atom. The NBO results predict the nitrogen bonding molecular orbitals to be in a ~ $sp^{1.6}$ state in phenyl-NCO versus a more sp-like state in phenyl-NCS indicating that chalcogen substitution causes a change in the nitrogen electronic environment.[12] While these studies have shown that structural changes occur as a result of chalcogen substitution, Fig. 1.1a) and 1.2a) also demonstrate that the side chain itself has an influence on the nitrogen electronic environment as a CNC bond angle of ~ 135.2° was derived for phenyl-NCO versus a ~ 140.7° bond angle for HCCNCO.[11,12] As the observance of

either phenomena has not been extensively studied, this warranted further investigation into how different structural changes influence the electronic environment around nitrogen and forms the justification for the work done in this thesis.[10–12]

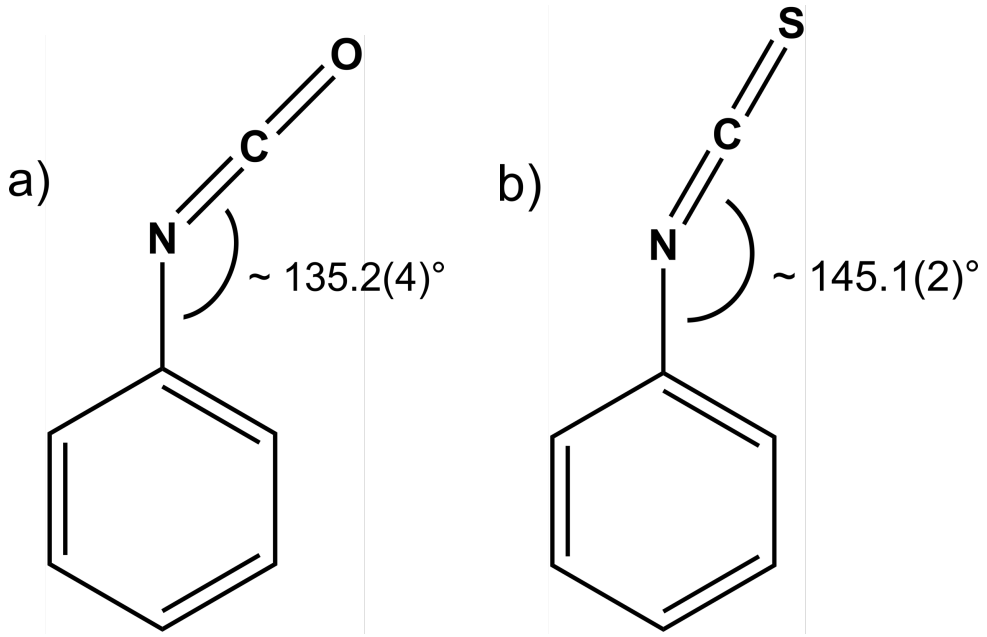

Fig. 1.2 Chemical structure of a) phenyl-NCO and b) phenyl-NCS highlighting the experimentally derived CNC bond angle for both molecules.

More recently, a microwave study by the van Wijngaarden group on allyl-NCO included a derivation of the molecular structure of its lowest energy conformer and this provided an opportunity to further probe how chalcogen substitution influences the electronic environment around nitrogen.[13] To accomplish this, the microwave spectrum of allyl-NCS (whose connectivity diagram is shown in Fig. 1.3) was studied as part of this thesis aided by quantum chemical calculations. Transitions were assigned to the parent species as well as the minor isotopologues which allowed for the structural derivation required to determine the extent of the structural changes due to chalcogen substitution.[10–13]

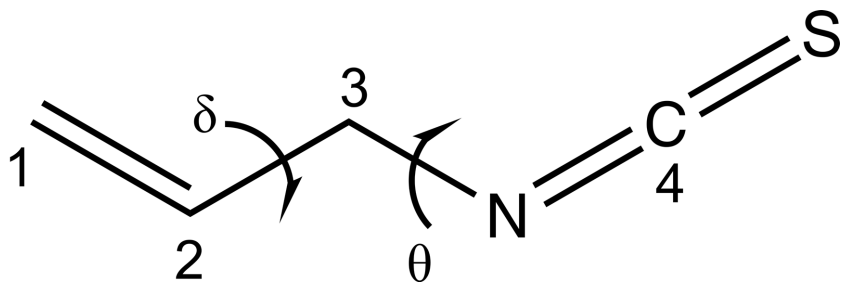

Fig. 1.3 Connectivity diagram of allyl-NCS in which all carbon atoms are numbered and the dihedral angles δ (C_1-C_2-C_3-N) and θ (C_2-C_3-N-C_4) are labeled. In this figure, both dihedrals have a value of 180°.

To further probe the impact of the side chain structure on the nitrogen electronic environment, the work done in this thesis was extended by conducting a microwave study of benzyl-NCO where quantum chemical calculations were used to assign transitions in its rotational spectrum for the first time. A microwave study of benzyl-NCS was not conducted as the high boiling point (243.0°C[14]) made it difficult to put it into the gas phase so instead, a computational study was completed so that predicted changes due to chalcogen substitution could be determined for the benzyl group and how this relates to other R groups. The connectivity diagram of both benzyl-NCO and benzyl-NCS are shown in Fig. 1.4.

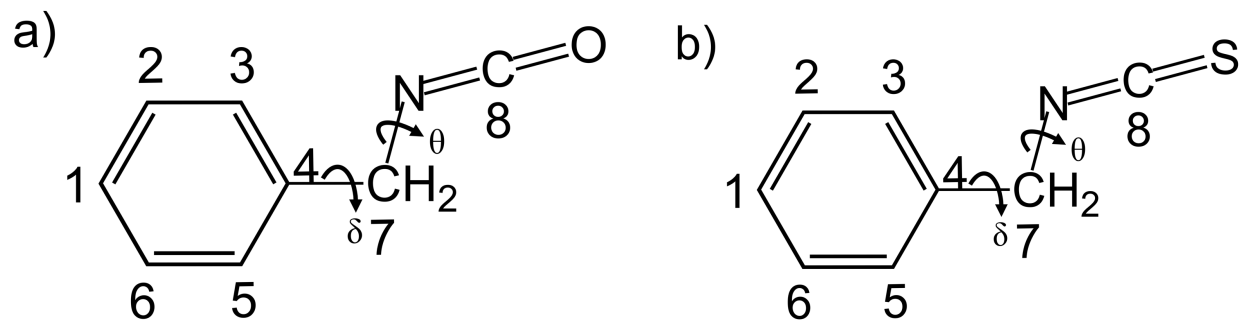

Fig. 1.4 Connectivity diagram of a) benzyl-NCO and b) benzyl-NCS in which all carbon atoms are numbered and the dihedral angles δ (C_5-C_4-C_7-N) and θ (C_4-C_7-N-C_8) are labelled. In this figure, both dihedrals have values of 180°.

1.3 Conformational Space and Microwave Spectroscopy

For allyl-NCS and both benzyl molecules, additional complexities arise that are not present in the other laboratory studies discussed above (aside from allyl-NCO) due to the two variable dihedral angles shown in Fig. 1.3 and 1.4. In the other compounds, only one variable dihedral is present making the conformational space easier to characterize by performing fast optimization calculations. However, the three molecules considered in this thesis can rearrange about two dihedrals (δ and θ) thereby generating a number of possible geometries. This required the construction of a three-dimensional potential energy surface (PES) to identify the stable geometries that contribute to the conformational landscape. Once a PES is constructed, the rest of the experimental procedure follows that of other gas phase microwave experiments such as the phenyl-NCO and phenyl-NCS study aside from the fact that there may be additional transitions in the rotational spectrum due to metastable conformers as well as their corresponding minor isotopologues.[12]

Since rotational transitions arise not only due to different molecules but due to different conformations of the same molecule as well, the rotational spectrum can therefore act as a fingerprint to identify both molecules and conformers which is critical to exploring the conformational space of the species studied in this thesis.[15] Furthermore, as transition frequencies also depend on mass, minor isotopologue transitions will occur at unique frequencies which allows for the derivation of the molecular structures required to examine changes due to both chalcogen and side chain substitution.[15] For these conformational studies, microwave spectroscopy is an ideal tool as the spacings between the unique rotational energy levels of each species correspond to frequencies in the microwave region of the electromagnetic spectrum.

1.4 Moments of Inertia

The primary influence on the microwave spectrum of a molecule is the moments of inertia associated with the rotation of that molecule about three mutually perpendicular axes (labeled a, b and c) originating from the center of mass and are referred to as I_a, I_b, and I_c, respectively.[15] In general, the moment of inertia associated with a given rotational axis is defined according to Eq. 1.1

$$I = \sum_i m_i r_i^2 \qquad \text{Eq. 1.1}$$

where m_i is the mass of atom i and r_i is the distance of atom i from the rotational axis.[15] The magnitude of the three moments of inertia with respect to each other dictates the classification of the rotor and examples of some of the different types of rotors are listed below along with the associated moments of inertia relationships.[15]

$I_c = I_b > I_a = 0$ Linear Rotor Eq. 1.2

$I_c = I_b = I_a$ Spherical Rotor Eq. 1.3

$I_c > I_b = I_a$ Oblate Symmetric Top Rotor Eq. 1.4

$I_c = I_b > I_a$ Prolate Symmetric Top Rotor Eq. 1.5

However, most molecules, including the three studied in this thesis, are classified as asymmetric top rotors in which the three moments of inertia are non-zero and non-equal.[15] Within the asymmetric rotor designation, a molecule can be further classified as either a prolate or oblate near-symmetric top rotor based on the following relationships.[15]

$I_c > I_b \approx I_a$ Oblate Near-Symmetric Top Rotor Eq. 1.6

$I_c \approx I_b > I_a$ Prolate Near-Symmetric Top Rotor Eq. 1.7

1.5 Rotational Constants and Transition Frequency Equations

The moments of inertia impact the rotational energy levels and rotational transition frequencies and in order to demonstrate this, consider the simplest case of a diatomic molecule. Since a diatomic molecule is an example of a linear rotor, Eq. 1.2 dictates that one moment of inertia will be zero while the other two will be equal and non-zero. The energy of the rotational energy levels (E_r) is described by Eq. 1.8 where h is Planck's constant and J is the rotational quantum number which can have any positive integer value.[15]

$$E_r = \frac{h^2}{8\pi^2 I_b} J(J+1) \qquad \text{Eq. 1.8}$$

The term values for a given J level (F(J)) can then be determined in frequency units by dividing the energy by Planck's constant to give Eq. 1.9. This equation can be simplified by setting $\frac{h}{8\pi^2 I_b}$ equal to B where B is defined as the rotational constant associated with the moment of inertia I_b

and is typically written in units of MHz.[15] Applying this substitution to Eq. 1.9 results in Eq. 1.10.[15]

$$F(J) = \frac{E_r}{h} = \frac{h}{8\pi^2 I_b} J(J+1) \qquad \text{Eq. 1.9}$$

$$F(J) = BJ(J+1) \qquad \text{Eq. 1.10}$$

It should be mentioned that only one rotational constant is required to describe the energy levels since Eq. 1.2 shows that linear rotors have only one unique, non-zero moment of inertia due to symmetry.[15] However, the molecules considered in this thesis are examples of asymmetric rotors meaning that there will be three distinct, non-zero moments of inertia and that two additional rotational constants (A and C) are also required to describe the rotational energy levels.[15] These rotational constants are calculated in the same form as the rotational constant B using the moment of inertia associated with their corresponding rotational axis.[15]

When considering molecules of lower symmetry than a linear rotor, there are additional complexities that arise in the term value equations. For a symmetric top rotor, this means that projections of the angular momentum vector onto the a (prolate symmetric rotor) or c (oblate symmetric rotor) rotational axis must be considered which is achieved by the inclusion of the quantum number K which can have any positive integer value from 0 to J.[15] For an asymmetric top rotor, projections of the angular momentum vector onto both the a and c rotational axes would be required and this, in principle, could be accounted for by the use of a separate K quantum number for both axes but these are not good quantum numbers as they do not commute with the rotational Hamiltonian simultaneously.[15] The consequence is that there is no exact equation to define the energy levels of an asymmetric rotor and so instead, these K quantum numbers are

obtained by approximating the term value equation for the asymmetric rotor at the prolate (K_a) or oblate (K_c) symmetric rotor limits as a numeric solution.[15]

In the rotational spectrum of a given molecule, transitions between energy levels is what is measured rather than the energy levels or the term values directly. For the example of a diatomic molecule, the transition frequency equation can be derived using Eq. 1.10 as a starting point along with the $\Delta J = \pm 1$ selection rule that restricts allowed rotational transitions to those involving adjacent energy levels.[15] Transition frequencies are then determined by subtracting the term value associated with the J+1 rotational energy level by the term value associated with the J rotational energy level to give Eq. 1.11 where ν represents the transition frequency.[15]

$$\nu = F(J+1) - F(J) = B(J+1)(J+2) - BJ(J+1) = 2B(J+1) \qquad \text{Eq. 1.11}$$

Eq. 1.11 therefore demonstrates that the transition frequencies of a diatomic molecule are separated by 2B whose value is dictated by the moment of inertia via the rotational constant B. For an asymmetric top rotor, the transition frequency patterns are much more complicated than this as the transition frequencies depend on all three rotational constants A, B and C. Moreover, it is also evident from Eq. 1.1 that the moment(s) of inertia depend upon atomic masses and positions meaning that the rotational transition frequencies are not only unique to different molecules but are also unique to different conformations of the same molecule as discussed earlier.[15] This therefore demonstrates the ability of the rotational spectrum to act as a fingerprint for different conformers when studying the conformational space of a given sample.

1.6 Selection Rules

To begin a discussion on the conditions for the observation of rotational transitions, once again consider the simple case of a diatomic molecule. As discussed above, transitions between

rotational energy levels are governed by the $\Delta J = \pm 1$ selection rule meaning that transitions must occur between adjacent energy levels.[15] Additionally, a second requirement is that the molecule must have a non-zero electric dipole moment in order for the molecule to rotate in phase with the oscillating electric field from incoming microwave radiation which will induce a transition between rotational energy levels.[15] A sample rotational energy level diagram showing rotational transitions and the corresponding transition frequencies is given in Fig. 1.5.[16]

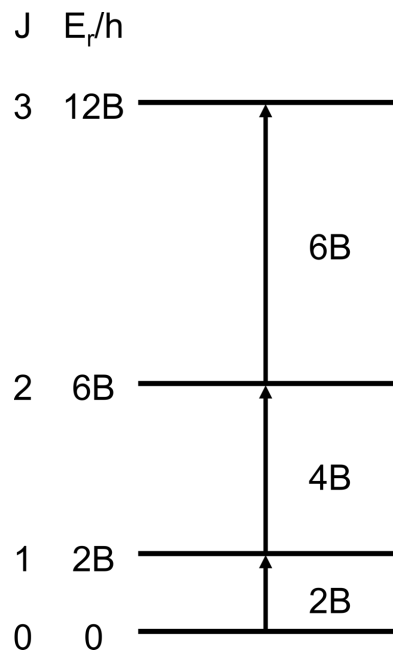

Fig. 1.5 Energy level diagram for a linear rotor showing the rotational transitions and the corresponding frequency values. The spacing between energy levels in this diagram is not to scale.

For a prolate or oblate symmetric top rotor, the linear rotor selection rules also apply in addition to the $\Delta K = 0$ selection rule which mandates that transitions between energy levels must occur within the same K band.[16] Lastly, consider an asymmetric rotor whose energy level diagram is shown in Fig. 1.6.[16] As a result of the inclusion of two K quantum numbers, there exists selection

rules for both K_a and K_c leading to three different types of allowed transitions (a-type, b-type and c-type) and one of each is shown in Fig. 1.7 between the J = 0 and J = 1 energy levels.[16]

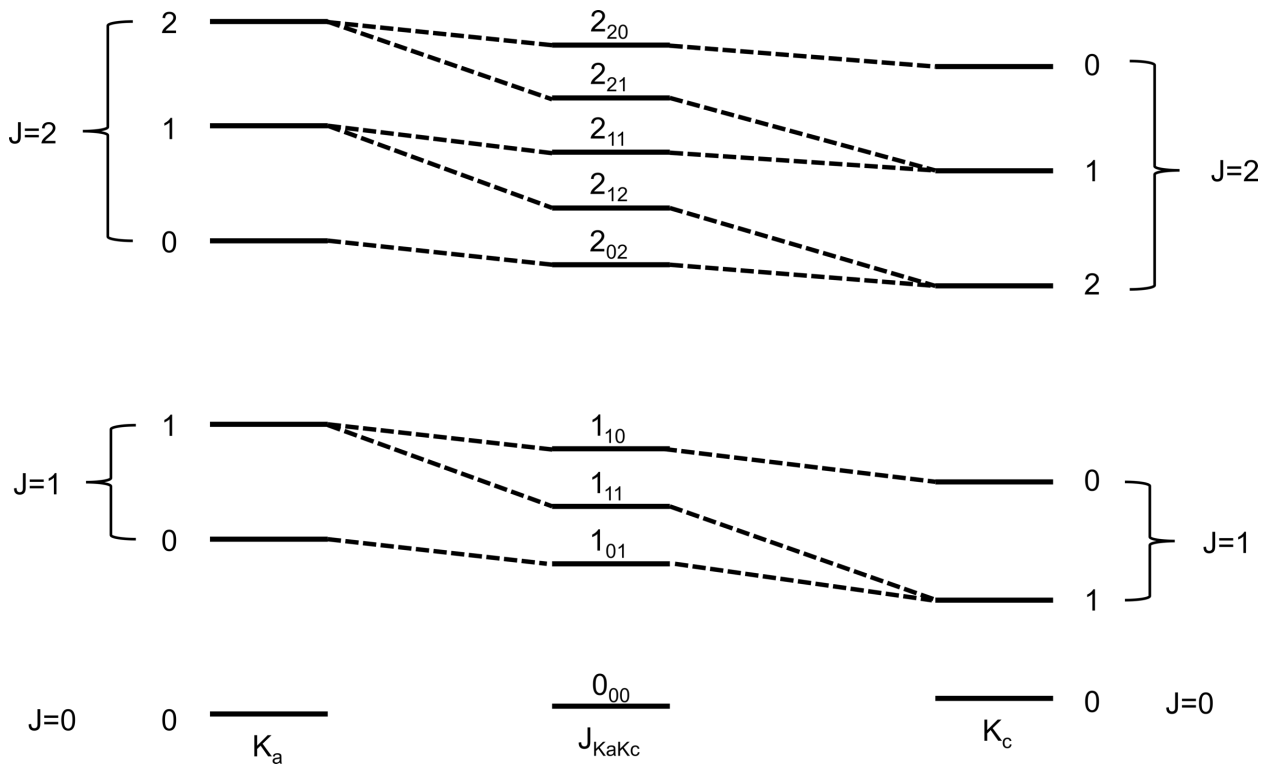

Fig. 1.6 Asymmetric rotor energy level diagram (middle) correlated to the prolate (left) and oblate (right) symmetric top limits. In this diagram, the spacings between rotational energy levels is not to scale.

While it is still true that $\Delta J = \pm 1$ for an asymmetric rotor and that the asymmetric rotor must also have a permanent electric dipole moment, there exists separate selection rules for the components of the overall dipole moment along the three rotational axes depending on what type of transition is considered.[16] In order for an a-type transition to be observed, the component of the electric dipole along the a-axis (μ_a) must be non-zero, and the change in K quantum numbers must be $\Delta K_a = 0$ ($\pm 2, \pm 4, \ldots$) and $\Delta K_c = \pm 1$ ($\pm 3, \pm 5, \ldots$).[16] Similar selection rules also apply to c-type transitions in that the dipole moment component along the c-axis (μ_c) must be non-zero but the

selection rules for K_a and K_c are switched such that $\Delta K_a = \pm 1(\pm 3, \pm 5, \ldots)$ and $\Delta K_c = 0\ (\pm 2, \pm 4, \ldots)$.[16] For b-type transitions, the corresponding dipole moment component along the b-axis (μ_b) must be non-zero and both K quantum numbers follow the $\Delta K = \pm 1(\pm 3, \pm 5, \ldots)$ selection rule.[16]

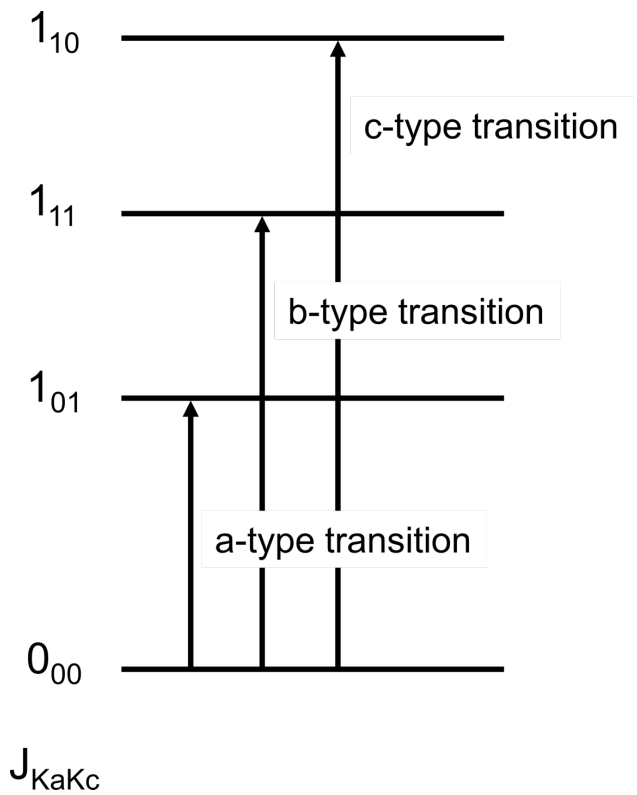

Fig. 1.7 A section of the asymmetric rotor energy level diagram showing an example of a, b and c-type transitions between the J = 0 and the J = 1 rotational energy levels. The spacings between energy levels is not to scale.

1.7 Centrifugal Distortion

As seen in Eq. 1.11, rotational transition frequencies are predicted to be 2B apart for a diatomic molecule regardless of the energy levels considered.[15] While this assumption is reasonable for lower rotational energy levels, at higher energies, centrifugal forces cause the atoms to move apart during rotation. This leads to an increase in atomic distances which increases in the

moments of inertia at higher J values and results in a decrease in the spacing between energy levels at higher J values.[15] This can be corrected by inserting the quartic centrifugal distortion constant D into Eq. 1.10 to give a new term value equation associated with the rotational energy level J that is shown in Eq. 1.12 where the energy level is lowered more as J increases and distortion effects grow.[15] Once again, the transition frequencies are calculated by subtracting Eq. 1.12 for the J+1 state by the term value associated with the rotational energy level J to give Eq. 1.13.

$$F(J) = BJ(J+1) - DJ^2(J+1)^2 \qquad \text{Eq. 1.12}$$

$$\nu = 2B(J+1) - 4D(J+1)^3 \qquad \text{Eq. 1.13}$$

For asymmetric tops like the ones studied in this thesis, additional distortion constants are needed as all bond lengths and angles may distort during rotation. As in the rigid rotor case, there are no exact energy expressions for asymmetric top rotors but for near symmetric tops, five quartic distortion constants are used to correct the energy levels and are given the symbols D_J, D_K, D_{JK}, d_1 and d_2.

1.8 ^{14}N Quadrupole Hyperfine Splitting

For molecules with nuclei that have a spin I=1 or greater, the non-spherical nuclear charge produces a non-zero nuclear quadrupole moment that interacts with the electric field gradient of the surrounding electrons.[17] This leads to an additional splitting (referred to as nuclear quadrupole hyperfine splitting) in the rotational spectrum.[17] This hyperfine splitting is labeled by the quantum number F and may take values according to Eq. 1.14 where I represents the nuclear spin.[17]

$$F = J + I, J + I - 1, \ldots, |J - I| \qquad \text{Eq. 1.14}$$

Lastly, transitions between hyperfine components from different energy levels are governed by the F quantum number selection rule which states that $\Delta F = 0, \pm 1$.[17]

In this work, allyl-NCS, benzyl-NCO and benzyl-NCS are molecules that contain one quadrupolar ^{14}N nucleus which has a nuclear spin of 1.[18] According to Eq. 1.14, this results in the quantum number F having three possible values for rotational energy levels above J=0. An example of the hyperfine structure is shown in Fig. 1.8 for the 2_{12} rotational energy level where J=2.[17]

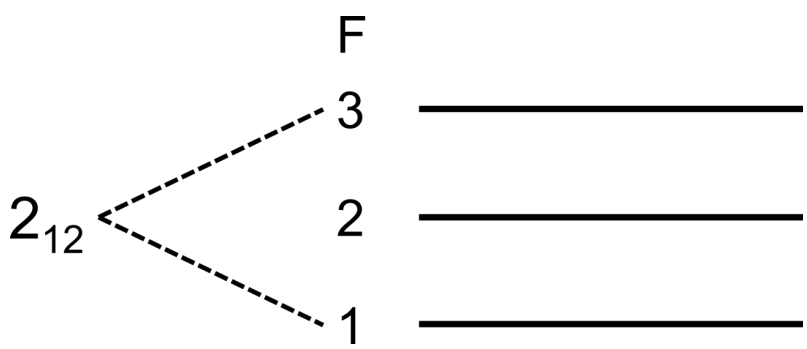

Fig. 1.8 Energy level diagram showing the hyperfine structure for the 2_{12} rotational energy level. The spacings between hyperfine components is not to scale.

Overall, this chapter has outlined how changes in molecular geometry lead to different rotational constants and transition frequencies which allows the rotational spectrum to act as a fingerprint when understanding the conformational landscape of a given species.[15] Furthermore, this chapter also discussed the additional quantum numbers required to describe the rotational energy levels for non-linear rotors and the selection rules that dictate which transitions are allowed.[15,16] Lastly, this chapter concluded with a discussion of the corrections required due to centrifugal distortion as well as the additional splitting that arises due to the quadrupolar ^{14}N nucleus that is present in the three molecules studied in this thesis.[15,17,18] The following chapter

will discuss the instrumentation and computational tools used to collect and analyze the rotational spectrum of allyl-NCS and benzyl-NCO in addition to the computational methods used to produce a calculated structure of benzyl-NCS in order to determine how changes in the terminal chalcogen and the side chain structure impact the electronic environment around nitrogen in such compounds.

References

(1) Interstellar medium https://www.britannica.com/science/interstellar-medium (accessed Mar 18, 2020).

(2) Snyder, L. E.; Buhl, D. Interstellar Methylacetylene and Isocyanic Acid. *Nat. Phys. Sci.* **1973**, *243* (125), 45–46.

(3) Kewley, R.; Sastry, K. V. L. N.; Winnewisser, M. The Millimeter Wave Spectra of Lsocyanic and Lsothiocyanic Acids. *J. Mol. Spectrosc.* **1963**, *10*, 418–441.

(4) Frerking, M. A.; Linke, R. A.; Thaddeus, P. Interstellar Isothiocyanic Acid. *Astrophys. J.* **1979**, *234*, L143–L145.

(5) Brünken, S.; Belloche, A.; Martín, S.; Verheyen, L.; Menten, K. M. Interstellar HOCN in the Galactic Center Region. *Astron. Astrophys.* **2010**, *516*, A109.

(6) Brünken, S.; Gottlieb, C. A.; McCarthy, M. C.; Thaddeus, P. Laboratory Detection of HOCN and Tentative Identification in Sgr B2. *Astrophys. J.* **2009**, *697* (1), 880–885.

(7) Halfen, D. T.; Ziurys, L. M.; Brünken, S.; Gottlieb, C. A.; McCarthy, M. C.; Thaddeus, P. Detection of a New Interstellar Molecule: Thiocyanic Acid HSCN. *Astrophys. J.* **2009**, *702* (2), L124–L127.

(8) Brünken, S.; Yu, Z.; Gottlieb, C. A.; McCarthy, M. C.; Thaddeus, P. Laboratory Detection of Thiocyanic Acid HSCN. *Astrophys. J.* **2009**, *706* (2), 1588–1593.

(9) Halfen, D. T.; Ilyushin, V. V.; Ziurys, L. M. Interstellar Detection of Methyl Isocyanate CH3NCO in Sgr B2(N): A Link From Molecular Clouds to Comets. *Astrophys. J. Lett.* **2015**, *812* (1), L5.

(10) Sun, W.; Davis, R. L.; Thorwirth, S.; Harding, M. E.; van Wijngaarden, J. A Highly Flexible Molecule: The Peculiar Case of Ethynyl Isothiocyanate HCCNCS. *J. Chem. Phys.* **2018**, *149* (10), 104304.

(11) Ross, S. C.; Cooper, T. A.; Firth, S.; Kroto, H. W.; Walton, D. R. M. The Microwave Spectrum and Semirigid Bender Analysis of Isocyanatoethyne, HCCNCO. *J. Mol. Spectrosc.* **1992**, *152*, 152–167.

(12) Sun, W.; Silva, W. G. D. P.; van Wijngaarden, J. Rotational Spectra and Structures of Phenyl Isocyanate and Phenyl Isothiocyanate. *J. Phys. Chem. A.* **2019**, *123* (12), 2351–2360.

(13) Sun, W.; Sogeke, O. P.; Silva, W. G. D. P.; van Wijngaarden, J. Dispersion-Driven Conformational Preference in the Gas Phase: Microwave Spectroscopic and Theoretical Study of Allyl Isocyanate. *J. Chem. Phys.* **2019**, *151* (19), 194304.

(14) Fisher Scientific. Benzyl isothiocyanate, 98%, ACROS Organics https://www.fishersci.com/shop/products/benzyl-isothiocyanate-98-acros-organics-3/AC402130050 (accessed Jan 29, 2020).

(15) Hollas, J. M. *Modern Spectroscopy*, Fourth Ed.; John Wiley & Sons Ltd: Chichester, 2004.

(16) Bernath, P. F. *Spectra of Atoms and Molecules*, 3rd. Ed.; Oxford University Press, 2016.

(17) Gordy, W.; Cook, R. L. *Microwave Molecular Spectra*, 3rd Ed.; John Wiley & Sons Inc.: New York, 1984.

(18) Lide, D. R.; Berger, L. I.; Covington, A. K.; Fox, R. B.; Frederikse, H. P. R.; Fuhr, J. R.; Goldberg, R. N.; Gschneidner, K. A.; Hammond, C. R.; Hampson, R. F.; et al. *CRC Handbook of*

Chemistry and Physics 84th Edition 2003-2004, 84th Ed.; CRC Press LLC, 2004.

Chapter 2. Experimental and Computational Methods

The following chapter addresses the instrumentation used to collect the rotational spectra of the molecules of interest in addition to the computer software utilized to conduct spectral and structural analyses. It will start with a conversation on the computational tools used predict the rotational spectra of allyl-NCS, benzyl-NCO and benzyl-NCS and procced by highlighting the programs that were required to provide an explanation of the relative energy ordering of the minima. This chapter will continue with a discussion on the delivery of a gaseous sample into a high vacuum chamber via a supersonic jet expansion. Afterwards, the instrumentation used to collect the rotational spectra of allyl-NCS and benzyl-NCO will be addressed along with the software used to fit the resulting spectra and perform structural analyses. Lastly, this chapter will conclude with an outline of the typical workflow for a microwave spectroscopy project.

2.1 Computational Methods

As a first step for each molecule studied, quantum chemical calculations were done in order to simulate the rotational spectra of allyl-NCS and benzyl-NCO in addition to modeling the benzyl-NCS conformational landscape. These calculations, all of which were done using the Gaussian 16 Revision B.01 program[1], commenced with two-dimensional scans where the electronic energy is calculated while changing the value of the two dihedral angles δ and θ and allowing all other structural parameters to be varied in order to minimize the energy. The resulting 3D PES for each molecule was used to identify low energy conformers that were then optimized by varying all structural parameters in order to obtain the lowest possible electronic energy. As shown in chapter 1, the molecular geometry impacts the rotational spectrum through the moments of inertia and therefore, these optimizations were required in order to calculate the rotational constants required to assign transitions in the rotational spectrum to a given conformer. Frequency calculations were

also conducted on the optimized minima to confirm that a true minimum was found through the absence of imaginary frequencies in addition to computing the centrifugal distortion constants required to account for the fact that the molecules considered could not be approximated as rigid rotors. Furthermore, optimization calculations were also carried out on suspected transition states with frequency calculations done to confirm that a transition state had been identified through the calculation of only one imaginary frequency. For allyl-NCS, the three-dimensional PES was complex enough such that before optimizing, suspected transition states needed to be identified by conducting scan calculations in which the value of only one dihedral was changed while all other parameters were allowed to vary. The frequency calculations done on the minima and the corresponding transition states were able to provide electronic energies with zero-point energy (ZPE) corrections that were used to provide a more accurate estimate of the heights of conformer interconversion barriers.

Additionally, the NBO 6.0[2] (for allyl-NCS) and NBO 7.0[3] (for benzyl-NCO and benzyl-NCS) routines were used to conduct a natural bond orbital (NBO) analysis of the global minima at the level of theory that provided closest agreement with the experimentally fit spectroscopic constants in order to determine the electronic structure of each molecule. From the NBO analyses, the hybridization state of the nitrogen bonding molecular orbitals was compared to examine the impact of either R group or chalcogen substitution. Lastly, to examine whether the bias of the benzyl-NCO conformational equilibrium towards the lowest energy conformer is caused by favourable intramolecular interactions, the program NCIPLOT[4] was used to conduct a noncovalent interactions (NCI) analysis. A NCI analysis was not conducted on the allyl-NCS and benzyl-NCS global minimum conformers as the optimized geometries were not consistent with the presence of an intramolecular interaction.

2.2 Sample Preparation and Supersonic Jet Expansion

Ahead of a discussion on the instrumentation used to collect the rotational spectra, the procedure of sample introduction into a vacuum chamber that is common to both the cp-FTMW and FTMW spectrometers should be discussed. For both instruments, a gas mixture containing the desired sample in neon buffer gas is carried towards a pulsed nozzle at 20 psi. The resulting gas mixture passes through the nozzle body where collisions between the buffer gas and the sample cool the sample to a rotational temperature of ~ 5 K.[5] Afterwards, the gas mixture enters the high vacuum chamber (~1 μTorr) where the pressure gradient between the nozzle and the chamber creates a supersonic jet expansion[6] which increases the median velocity of the sample molecules while at the same time, narrowing the velocity distribution such that the sample molecules travel in the same direction at essentially the same speed as they pass through the high vacuum chamber thereby preventing further collisons.[5]

Collecting the rotational spectrum of a low-pressure gaseous sample seeded in a buffer gas is advantageous in that any potential interactions with a solvent are removed. The resulting rotational spectrum will therefore more accurately reflect the conformational landscape of an isolated molecule by removing any bias in the conformational equilibrium that is not related to intramolecular interactions. An additional benefit of the supersonic jet expansion is that cooling the sample to a rotational temperature of ~ 5K leads to an increase in the population of the lowest lying rotational energy levels thereby simplifying the rotational spectrum. Furthermore, because the sample molecules are travelling at essentially the same velocity as they enter the chamber, they are able to avoid further collisions that would increase the population of higher energy rotational energy levels and complicate the rotational spectrum of the sample.[5] The simplified rotational spectrum also allows for a more accurate assignment of the less intense transitions including those

due to the heavy atom minor isotopologues associated with a given conformer which results in a more accurate experimentally derived structure. These aspects of the supersonic jet expansion make it essential to the assignment of transitions to the lowest energy conformers of allyl-NCS and benzyl-NCO.

2.3 Chirped pulse FTMW spectrometer

For both allyl-NCS and benzyl-NCO, the broadband rotational spectrum was obtained using the custom-built cp-FTMW spectrometer available in the van Wijngaarden lab[7] shown in Fig. 2.1 which was constructed based on a design by Brown et al. in 2008.[8] A corresponding schematic diagram describing the components for microwave excitation and detection is shown in Fig. 2.2.

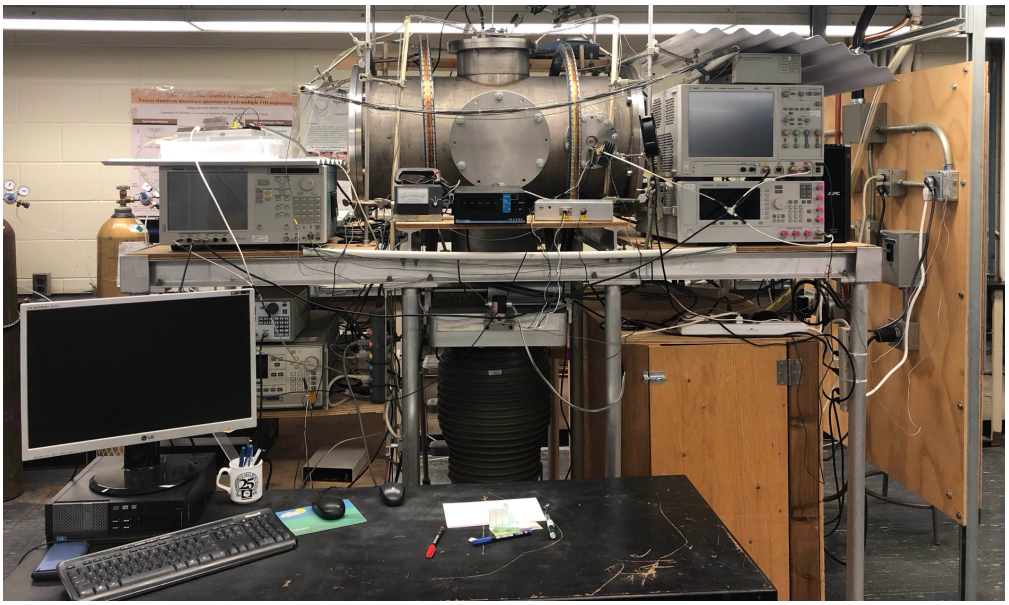

Fig. 2.1 An image of the 8-18 GHz cp-FTMW instrument in the van Wijngaarden lab.

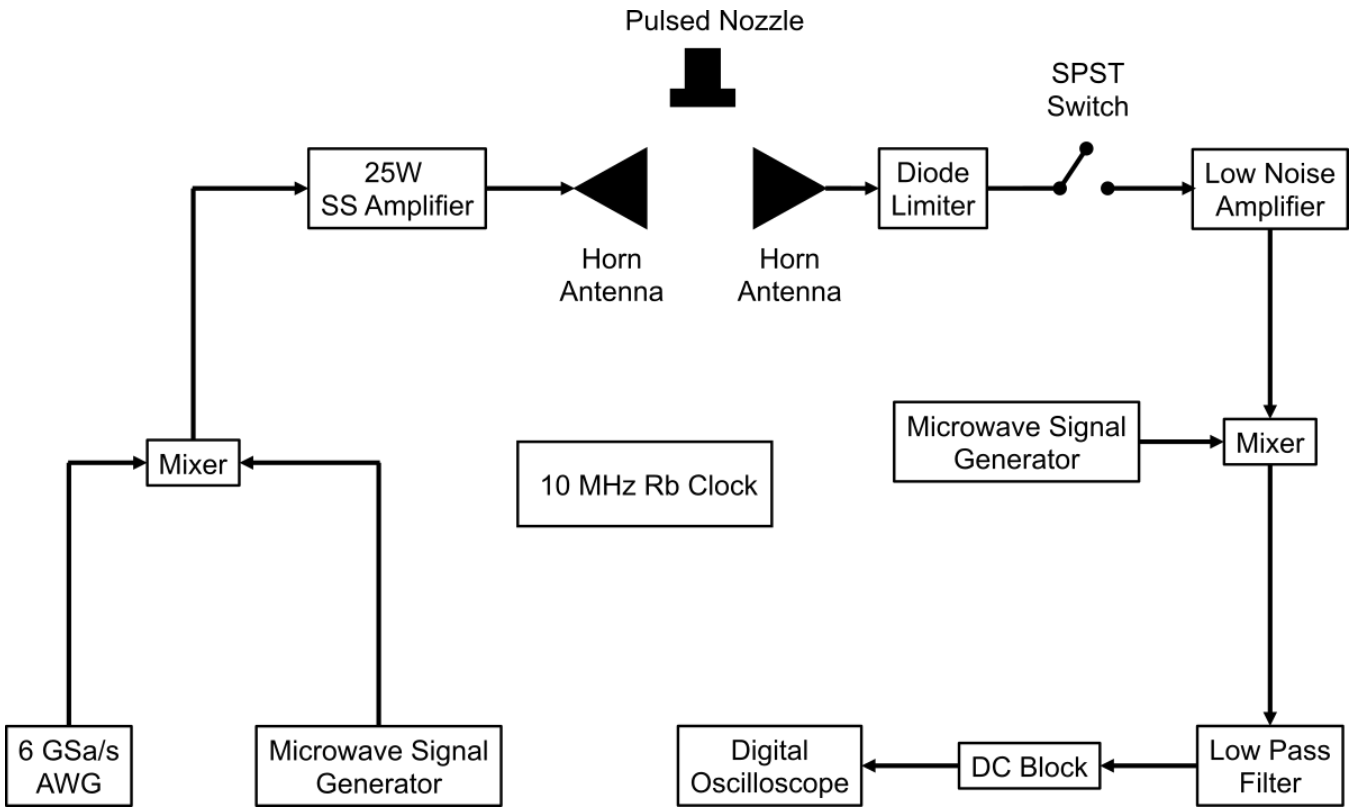

Fig. 2.2 A schematic diagram showing the electronic circuit of the cp-FTMW instrument.

This instrument, which was used to record 2 GHz segments of the rotational spectrum at a time works by first, mixing the output from a microwave signal generator which produces a centre microwave frequency with the output from an arbitrary waveform generator (AWG) which produces a rapid frequency sweep or "chirp" of 1 GHz above and below the target frequency in ~ 1-5 μs.[7] The resulting waveform is a microwave pulse centered at a selected frequency with two 1 GHz sidebands thereby forming a 2 GHz spanning microwave pulse. This microwave pulse is then amplified by a 25 W solid state (SS) amplifier before passing through a horn antenna inside a high vacuum chamber that is kept at a pressure of ~1 μTorr by a large (12 inch) diffusion pump aided by a pair of rotary vane pumps.[7] Inside the chamber, the microwave pulse interacts with the sample in the supersonic jet expansion that was described earlier. If the sample has a rotational transition

within the 2 GHz range of the chirped pulse, the electric dipoles of the molecules will align with the oscillating electric field and the molecules will rotate in phase at that frequency.

As the microwave pulse dissipates, the molecules relax from alignment and the resulting emission signal known as a free induction decay (FID) is collected using a second horn antenna at the opposite end of the high vacuum chamber. The emission signal then enters the detection circuit (which is protected from the excitation pulse by a diode limiter and a single pole single throw (SPST) switch) where it initially passes through a low noise amplifier. Following amplification, a mixer and second microwave signal generator is used to frequency downconvert the resulting FID signal which is then sent to a 6 GHz oscilloscope for digitization after a final filtration step using a low pass filter and DC blocker. Lastly, the emission signal, which is in the time domain, is transformed into the frequency domain by performing a fast Fourier transform (FFT) to produce a 2 GHz segment of the rotational spectrum of the species of interest. This segment can later be combined with other 2 GHz segments recorded at different centre frequencies to produce a broadband rotational spectrum from 8-18 GHz. For this instrument, the averaging of FIDs is made possible by the 10 MHz rubidium clock shown in Fig. 2.2 which keeps the oscilloscope, the AWG and the two microwave signal generators in phase.[7] The resulting broadband spectrum is then used to perform an initial assignment of the transitions due to different parent species and corresponding minor isotopologues for a given molecule. For the cp-FTMW spectrometer, transition line widths ≤ 200 kHz are observed at half maximum.

2.4 Balle-Flygare FTMW Spectrometer

After initially collecting the broadband rotational spectrum of a molecular species of interest using the cp-FTMW spectrometer, transitions were then collected using the custom-built FTMW spectrometer available in the van Wijngaarden lab.[9] This narrowband instrument was

constructed based on the design described by Balle and Flygare in 1981[10] and is shown in Fig. 2.3 along with a corresponding electronic circuit schematic diagram in Fig. 2.4.

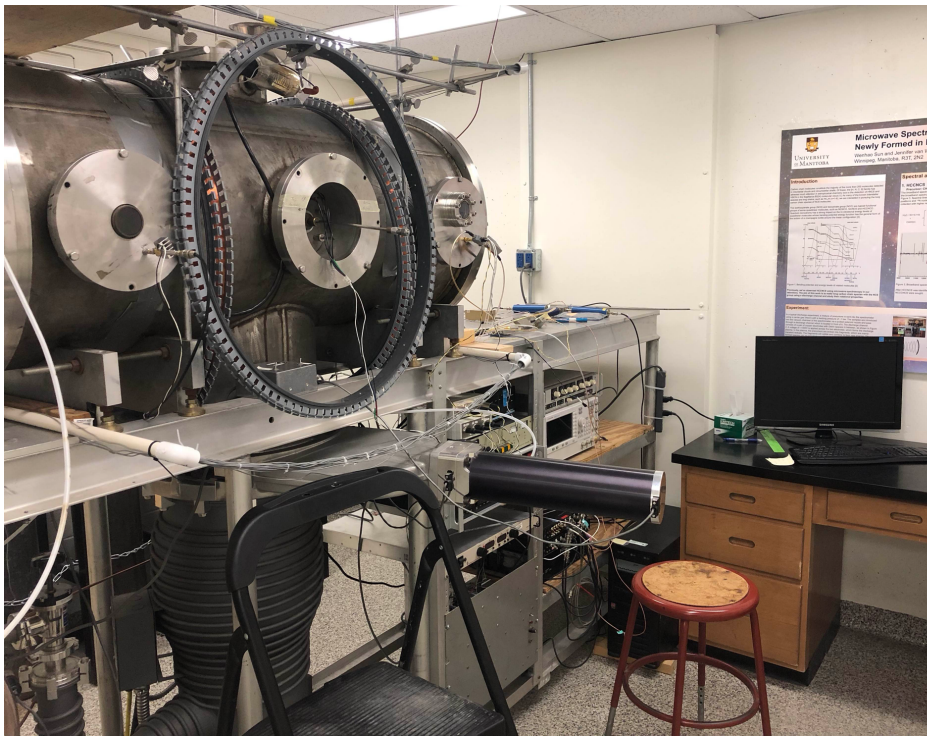

Fig. 2.3 An image of the custom-built FTMW spectrometer in the van Wijngaarden lab.

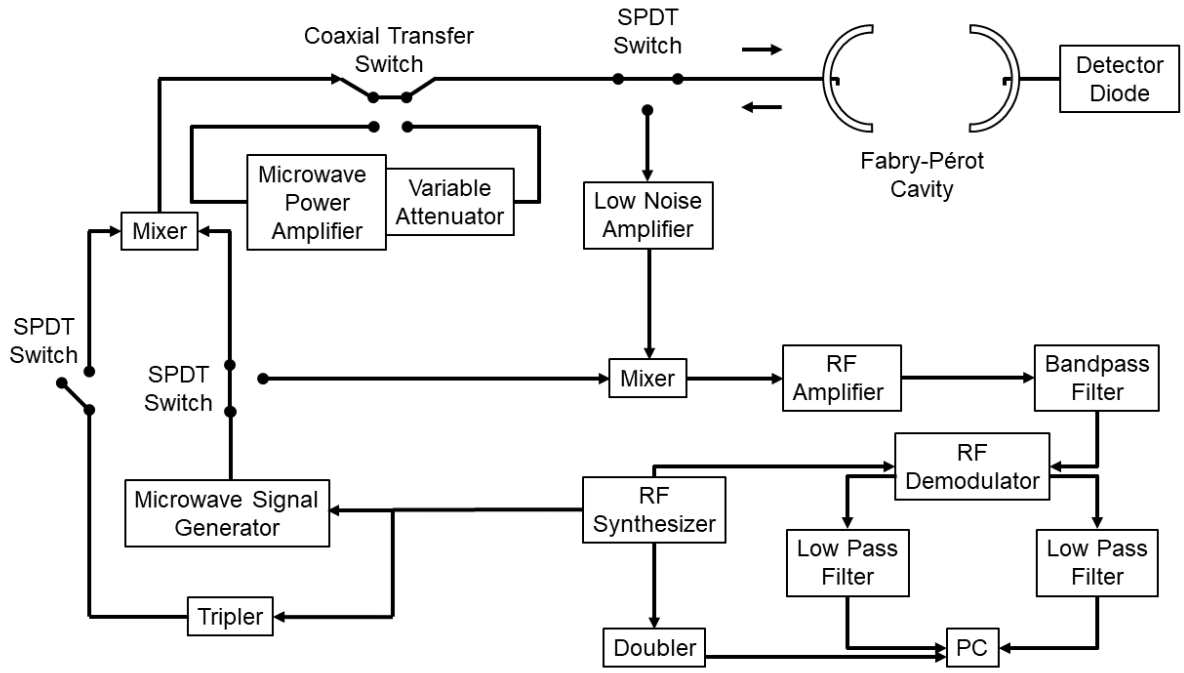

Fig. 2.4 A schematic diagram showing the electronic circuit of the FTMW instrument.

For the FTMW spectrometer, a high resolution 1 MHz segment of the rotational spectrum is collected by first, using a microwave signal generator to produce microwave radiation at a frequency that is 30 MHz lower than the frequency of interest. The remaining 30 MHz comes in the form of 10 MHz from a radiofrequency (RF) synthesizer which is tripled and then mixed with the output from the microwave signal generator to form radiation with a single sideband at the desired frequency. The resulting microwave radiation passes through a coaxial transfer switch used to separate the excitation and cavity tuning circuits and then through a single pole double throw (SPDT) switch used to separate the excitation and detection circuits. Afterwards, a wire hook antenna at the center of the moveable aluminum mirror is used to introduce the microwave radiation into the Fabry-Pérot cavity whose length is tuned by a servo motor adjusting the position of the moveable mirror relative to the stationary mirror such that the cavity is in resonance with

the frequency of the microwave pulse. The Fabry-Pérot cavity is kept at a pressure of ~1 μTorr by a diffusion pump aided by a large rotary vane pump.

Once the microwave pulse interacts with the supersonic jet, the weak emission signal produced as the molecules relax from alignment is collected by the antenna in the moveable mirror and moves towards the SPDT switch which is now open towards the detection circuit. Signal processing then begins by an initial amplification using a low noise amplifier followed by a mixing of the amplified signal with radiation from the microwave signal generator that is offset by 30 MHz. Afterwards, the frequency downconverted signal is further amplified via a RF amplifier and filtered using a bandpass filter. The remaining signal then enters a RF demodulator where it undergoes a second downconversion by mixing it with 27.5 MHz radiation from the same RF synthesizer used to create the sideband of the excitation radiation. A final filtration of the emission signal is done using a pair of low pass filters after which, the signal is digitized. Lastly, a FFT is applied to the digitized signal thereby producing a 1 MHz segment of the rotational spectrum.[9] In the resulting spectrum, a doublet is seen where only one rotational transition is expected. This splitting, known as Doppler splitting, is caused by the molecular beam running parallel to the detection antenna and to overcome this, the center frequency between the two components is recorded as the "true" transition frequency. Additionally, the internal clock of the RF synthesizer shown in Fig. 2.4 acts as a reference for both the excitation and detection circuits of the FTMW spectrometer which allows for the phase-coherent averaging of multiple FID signals until the spectrum has an adequate signal-to-noise ratio (SNR).[9] For this instrument, recorded rotational transitions have full linewidths of ~ 7 kHz at half maximum in addition to uncertainties of ± 2kHz in transition frequencies.

In general, a comparison of the two instruments reveals similarities such as the utilization of a supersonic jet expansion in both instruments and that once in the chamber, the sample is exposed to microwave radiation after which, the resulting FID is collected, filtered and then Fourier transformed into the frequency domain. Despite these similarities, there are differences between the two instruments such as the use of a cavity and constant frequency microwave radiation in the FTMW spectrometer. This allows for an increase in the FID amplitude giving the FTMW spectrometer the increased sensitivity required to observe low intensity transitions and to observe features such as ^{14}N hyperfine splitting, however, this instrument must also be tuned to each frequency and only produces 1 MHz segments of the rotational spectrum at a time.[8] On the other hand, the cp-FTMW spectrometer uses a chirped pulse to access transitions across a 2 GHz range of the rotational spectrum at once. While this allows for a quick search across a broad range of the spectrum, the transition intensities and frequencies are less precise as the resolution of the spectrometer is low enough for additional features such as ^{14}N hyperfine splitting to not be observable. Therefore, the cp-FTMW spectrometer is best used to perform an initial assignment of transitions in the rotational spectrum of a given sample while the FTMW spectrometer is better suited to record final transition frequencies and to assign the ^{14}N hyperfine structure.

2.5 Spectral and Structural Analysis

Transitions recorded using the FTMW spectrometer were fit via H.M. Pickett's least-squares fitting program SPFIT[11] in order to obtain a set of experimentally determined spectroscopic constants that describe the rotational energy levels of the molecules. For this program, either Watson's symmetrically[12] or asymmetrically[13] reduced Hamiltonian (S-reduced or A-reduced, respectively) can be used to fit the rotational transitions but because optimizations of allyl-NCS revealed similar calculated values for rotational constants B and C as was the case for

benzyl-NCO, these molecules were therefore predicted to be near symmetric top rotors which justified the use of Watson's S-reduced Hamiltonian in the I^r representation to fit the observed transitions. When fitting rotational transitions for both allyl-NCS and benzyl-NCO, all three rotational constants A, B and C were required as the two molecules are asymmetric rotors. Since the two molecules are also non-rigid rotors, distortion constants D_J, D_{JK}, D_K, d_1 and d_2 were included in order to account for this. Furthermore, as a result of the quadrupolar ^{14}N nucleus in both allyl-NCS and benzyl-NCO, hyperfine splitting is expected which required the inclusion of the quadrupolar coupling constants $1.5*\chi_{aa}$ and $0.25*(\chi_{bb}-\chi_{cc})$ when fitting rotational transitions. The quality of the resulting fits was evaluated based on a comparison of the experimentally fit spectroscopic constants to the corresponding calculated values and by examining the standard deviation in the experimentally fit constants as well as the magnitude of the root mean square (RMS) error in the overall fit.

For a given molecule, the rotational spectrum is influenced by the moments of inertia as discussed in chapter 1 which are themselves dependent on the conformer geometry and isotopic masses. Depending on intensities, transitions may be assigned to minor isotopologues in natural abundance which provides the possibility of deriving the molecular structure. In order to probe the impact of different side chains and chalcogen substitution on the nitrogen electronic environment, a structural analysis was performed using Kisiel's least squares fitting program STRFIT[14]. This program, which was constructed based on concepts described by R.H. Schwendeman[15], fits a ground state effective (r_0) structure by minimizing the difference between the calculated and experimental moments of inertia through an adjustment of selected structural parameters such as bond length and angles.[16] To derive the r_0 structure, STRFIT requires an approximate geometry as a starting point (in this case the calculated equilibrium (r_e) structure of a particular conformer was

used) along with the rotational constants of the parent species and the corresponding minor isotopologues (in addition to their atomic masses) in order to derive the r_0 structure.

2.6 General Microwave Study Timeline

Described below is the general timeline for the microwave study of allyl-NCS and benzyl-NCO. Initially, a three-dimensional potential energy surface (PES) is constructed for each molecule by calculating the electronic energy for different values of the dihedral angles δ and θ while allowing all other parameters to be varied. Constructing these surfaces took ~ 2-4 days to complete depending on the number of points and number of electrons. Minima identified on the resulting surfaces were then optimized to obtain the calculated spectroscopic constants and dipole moment components required to produce a simulated spectrum for each conformer. These calculations took an additional ~ 14 to 27.5 hours depending on the size of the molecule and number of electrons in the model. Next, the barriers to interconversion between conformers were estimated by optimizing the transition states which required as much as 16 hours of calculations for each molecule. However, due to the additional complexities of the allyl-NCS PES, ~ 3 days of computational time was spent on scan calculations used to identify possible transition states before such optimizations could be done. Lastly, to examine the change in hybridization of the nitrogen bonding orbitals as a result of R group or chalcogen substitution, a NBO analysis was conducted on the global minimum of allyl-NCO, allyl-NCS and both benzyl molecules which took ~ 5-50 minutes to complete for each molecule depending on the number of electrons.

After the optimization of all minima on a given PES, the cp-FTMW spectrometer was used to collect the broadband rotational spectrum of a desired molecule but before collection, a gas mixture containing the sample in argon was pulsed through the instrument for ~ 2 days in order to remove previous samples from the instrument tubing and to coat it with the new sample.

Afterwards, a new gas mixture was prepared containing the desired sample seeded in neon buffer gas and ~ 1 hour was spent adjusting different parameters in order to optimize the signal in the rotational spectrum. After the experimental parameters had been optimized, the rotational spectrum was then recorded in 2 GHz segments which took ~ 2.5 hours to obtain 1.5 million FIDs for each segment. Following this, the simulated spectra were used to visually assign transitions in the experimental spectrum to each conformer via the least-squares fitting program pgopher.[17] The spectroscopic constants from the preliminary fit along with the quadrupole coupling constants from the quantum chemical calculations were used as input for Picket's SPCAT program[11] which generated a more detailed set of predicted rotational transitions with hyperfine components.

Before recording transitions using the FTMW spectrometer, the sample manifold was conditioned in a procedure identical to the one used for the cp-FTMW spectrometer and also took ~ 2 days to complete. Afterwards, a new gas mixture was then prepared using neon as the buffer gas and another ~ 1 hour was spent adjusting various parameters to optimize the signal. Once optimized, transitions recorded in the broadband spectrum were then recollected using the FTMW spectrometer to obtain more precise transition frequencies and to record the expected hyperfine splitting due to the presence of the quadrupolar ^{14}N nucleus. This was achieved by tuning the cavity to each frequency and averaging over ~ 100-2000 cycles (~ 0.2-5 minutes) depending on transition intensity. After a few transitions were recollected and then fit using SPFIT, the improved constants were then used in combination with SPCAT to generate an updated list of predictions. Those updated predictions were then used to record additional transitions which were then also included in the least squares fit. This process was repeated several hours per day over the course of ~ 1 month until all observable transitions due to the parent species were assigned.

Following the assignment of transitions due to the parent species of a particular conformer, the process for assigning transitions to the corresponding minor isotopologues began by first, calculating their rotational constants via Kisiel's PMIFST program[14] which calculates rotational constants using the r_e structure as a starting point and then changes the mass of one atom at a time. The estimated constants were then scaled using the experimentally fit and calculated rotational constants of the parent species to obtain a better initial estimate of the isotopologue rotational constants. Afterwards, the rest of the procedure used to collect and fit the parent species transitions was also applied to the minor isotopologues, however, due to the low relative abundance of the minor isotopologues, the rotational transitions recorded using the FTMW spectrometer needed to be averaged longer compared to the parent species transitions of the same quantum numbers. This meant averaging each transition for ~ 500-30 000 cycles (1-71 minutes) which was determined by noting the number of cycles required to achieve an adequate SNR for the parent and accounting for the relative abundance of the isotopic species. For example, if a parent transition was recorded in 100 cycles, to achieve the same SNR, a transition of the same quantum numbers for a ^{13}C isotopologue (which is 1% abundant) would need to be averaged over 100/0.01 or 10 000 cycles. The procedure outlined for recording transitions due to the minor isotopologues occurred over a period of ~ 1-2 months depending on the number of conformers and the number of observable isotopologues for each conformer. After the observable transitions due to the parent species and heavy atom minor isotopologues were assigned, the r_0 structure was derived using all sets of rotational constants in combination with STRFIT in order to examine structural changes due to R group or chalcogen substitution.

References

(1) Frisch, M. J.; Trucks, G. W.; Schlegel, H. B.; Scuseria, G. E.; Robb, M. A.; Cheeseman, J. R.; Scalmani, G.; Barone, V.; Petersson, G. A.; Nakatsuji, H.; Li, X.; Caricato, M.; Marenich, A. V.; Bloino, J.; Janesko, B. G.; Gomperts, R.; Mennucci, B.; Hratch, D. J. Gaussian 16, Revision B.01. Gaussian, Inc.: Wallingford, CT 2016.

(2) Glendening, E. D.; Badenhoop, J. K.; Reed, A. E.; Carpenter, J. E.; Bohmann, J. A.; Morales, C. M.; Landis, C. R.; Weinhold, F. NBO 6.0. Theoretical Chemistry Institute, University of Wisconsin: Madison 2013.

(3) Glendening, E. D.; Badenhoop, J. K.; Reed, A. E.; Carpenter, J. E.; Bohmann, J. A.; Morales, C. M.; Karafiloglou, P.; Landis, C. R.; Weinhold, F. NBO 7.0. Theoretical Chemistry Institute, University of Wisconsin: Madison 2018.

(4) Contreras-García, J.; Johnson, E. R.; Keinan, S.; Chaudret, R.; Piquemal, J.-P.; Beratan, D. N.; Yang, W. NCIPLOT: A Program for Plotting Noncovalent Interaction Regions. *J. Chem. Theory. Comput.* **2011**, *7* (3), 625–632.

(5) Smalley, R. E.; Wharton, L.; Levy, D. H. Molecular Optical Spectroscopy with Supersonic Beams and Jets. *Accounts. Chem. Res.* **1977**, *10* (4), 139–145.

(6) Havenith, M. The Molecular Beam. In *Infrared Spectroscopy of Molecular Clusters*; Springer Berlin Heidelberg: Berlin, Heidelberg, 2002; Vol. 176, pp 35–46.

(7) Evangelisti, L.; Sedo, G.; van Wijngaarden, J. Rotational Spectrum of 1,1,1-Trifluoro-2-Butanone Using Chirped-Pulse Fourier Transform Microwave Spectroscopy. *J. Phys. Chem. A.* **2011**, *115* (5), 685–690.

(8) Brown, G. G.; Dian, B. C.; Douglass, K. O.; Geyer, S. M.; Shipman, S. T.; Pate, B. H. A Broadband Fourier Transform Microwave Spectrometer Based on Chirped Pulse Excitation. *Rev. Sci. Instrum.* **2008**, *79* (5), 053103.

(9) Sedo, G.; van Wijngaarden, J. Fourier Transform Microwave Spectra of a "New" Isomer of OCS-CO2. *J. Chem. Phys.* **2009**, *131* (4), 044303.

(10) Balle, T. J.; Flygare, W. H. Fabry–Perot Cavity Pulsed Fourier Transform Microwave Spectrometer with a Pulsed Nozzle Particle Source. *Rev. Sci. Instrum.* **1981**, *52* (1), 33.

(11) Pickett, H. M. The Fitting and Prediction of Vibration-Rotation Spectra with Spin Interactions. *J. Mol. Spectrosc.* **1991**, *148* (2), 371–377.

(12) Watson, J. K. G. *Vibration Spectra and Structure*; Durig, J., Ed.; Elsevier: Amsterdam, 1977.

(13) Watson, J. K. G. Determination of Centrifugal Distortion Coefficients of Asymmetric-Top Molecules. III. Sextic Coefficients. *J. Chem. Phys.* **1968**, *48* (10), 4517.

(14) Kisiel, Z. PROSPE - Programs for ROtational SPEctroscopy http://www.ifpan.edu.pl/~kisiel/prospe.htm (accessed Nov 8, 2019).

(15) Schwendeman, R. H. Structural Parameters from Rotational Spectra. In *Critical Evaluation of Chemical and Physical Structural Information*; Lide, D. R., Martin, Paul, A., Eds.; National Academy of Sciences: Washington, D.C., 1974; pp 94–115.

(16) Gordy, W.; Cook, R. L. *Microwave Molecular Spectra*, 3rd Ed.; John Wiley & Sons Inc.: New York, 1984.

(17) Western, C. M. PGOPHER, A Program for Simulating Rotational, Vibrational and

Electronic Spectra http://pgopher.chm.bris.ac.uk (accessed Jun 25, 2019).

Chapter 3. Microwave Spectroscopy and Computational Study of Allyl-NCS[2]

In this chapter, the microwave and computational study of allyl-NCS will be discussed. The results from this investigation are compared to those recently published by the van Wijngaarden group for allyl-NCO in order to determine the impact of oxygen to sulfur substitution on the molecular structure. After explaining these findings in terms of differences in nitrogen hybridization, structural changes for the allyl group are then compared to those reported for other R group structures in order to determine how the side chain influences the nitrogen electronic environment.

3.1 Abstract

The pure rotational spectrum of allyl isothiocyanate (CH_2=$CHCH_2$-NCS) was collected from 4-26 GHz using Fourier transform microwave (FTMW) spectroscopy. Its analysis revealed the presence of two conformers that arise due to variation in the CCCN and CCNC dihedral angles. The observed spectrum is consistent with the accompanying potential energy surfaces derived using quantum chemical calculations at the B3LYP-D3(BJ) and MP2 levels of theory. Together, this experimental and theoretical study unequivocally identifies a new conformer (I) as the global minimum geometry. The spectral assignment of this new conformer is verified by the observation of transitions consistent with its ^{34}S, ^{13}C and ^{15}N isotopologues and with the characteristic ^{14}N quadrupole hyperfine patterns. For conformer I, the substitution (r_s) and effective ground state (r_0) structures were derived and reveal contributions from a large amplitude motion in the CCNC angle. The remaining geometric parameters compare well with the equilibrium structure (r_e) from

[2] A copy of this work has been published in the Journal of Physical Chemistry A under the citation: Stitsky, J.; Silva, W. G. D. P.; Sun, W.; van Wijngaarden, J. Conformers of Allyl-Isothiocyanate: A Combined Microwave Spectroscopy and Computational Study. *J. Phys. Chem. A.* **2020**, *124* (19), 3876-3885. Copyright © 2020 American Chemical Society.

B3LYP-D3(BJ)/cc-pVQZ calculations. The derived CNC bond angle of 152.6(3)° for conformer I of allyl-NCS is found to be ~15° larger than that of allyl-NCO (137.5(4)°), which is in line with a change in the hybridization at nitrogen from an orbital with more ~sp character in allyl-NCS to ~$sp^{1.5}$ in allyl-NCO as determined via natural bond orbital analyses.

3.2 Introduction

The detection of gas phase NCO- and NCS-containing compounds in molecular clouds through the identification of their spectral fingerprints provides useful information for modelling the chemistry of the interstellar medium. Aided by laboratory-based high resolution rotational spectroscopy, the existence of HNCO,[1] HNCS,[2] HOCN,[3,4] HSCN[5,6] and CH_3NCO[7,8] in space have already been confirmed making the study of other NCO/NCS containing species of astronomical interest. Organic isothiocyanates, such as allyl-NCS (Fig. 1), are naturally occurring in plant cells where they are produced as a result of cellular damage,[9] and also have industrial applications such as in food preservation.[10] This class of compounds, therefore, is of broad chemical interest as components of diverse systems in both terrestrial and astronomical environments.

When compared to previously studied NCO/NCS-containing molecules, the allyl-substituted compounds present a more complex conformational landscape due to the additional methylene (CH_2) group in their backbone.[11] The rotational spectrum of allyl-NCO, for example,

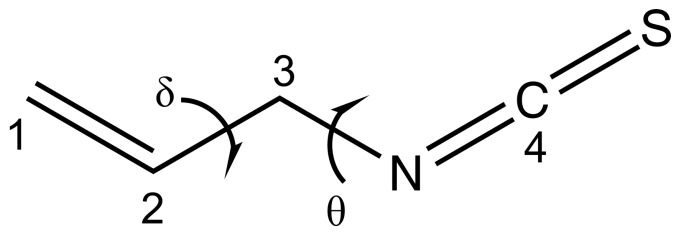

Fig. 3.1 Chemical structure of allyl-NCS showing dihedral angles δ (C_1-C_2-C_3-N) and θ (C_2-C_3-N-C_4). Both δ and θ are 180° in this image.

has been a puzzle in the literature for more than twenty-five years. Although two stable conformations, *cis* (δ= 0º and θ=180º) and *gauche* (δ= ~120º and θ=0º) were predicted, only the higher energy *gauche* conformer was observed via its rotational spectrum.[12,13] Recently, an accurate picture of the conformational space of allyl-NCO was derived by exploiting high-resolution Fourier transform microwave (FTMW) spectroscopy and dispersion-corrected density functional theory (DFT-D) calculations.[11] In addition to the previously reported *gauche* conformer, transitions consistent with a new global minimum geometry (conformer I) were observed. The derived potential energy surface furthermore confirmed that the *cis* conformer could undergo facile relaxation to conformer I in the molecular beam expansion.

In allyl-NCO,[11] the intramolecular dispersive interaction between the CH_2=CH- and NCO-groups was found to play a critical role in the conformational distribution as it led to the existence of conformer I. From previous spectroscopic reports involving allyl-NCS, the conformational story appears to mimic that found in the earlier studies of its oxygen analog. Using Stark-modulated microwave spectroscopy,[14,15] a *gauche* conformer was reported for allyl-NCS while a purported lower energy *cis* conformer based on ^{13}C NMR experiments[16] was not observed. Based on this, it is clear that the conformational space of allyl-NCS requires further study to explore whether a new, dispersion-stabilized conformer is present and how the change from oxygen to sulfur influences the conformational equilibrium.

Rotational studies on isocyanates and isothiocyanates, in general, not only identify stable conformers, but also afford the opportunity to investigate the influence of the terminal chalcogen atom on the electronic environment around the nitrogen atom. Comparison of the geometries of HCCNCO[17] and HCCNCS,[18] for example, have shown that changing from oxygen to sulfur results in an increase in the CNC bond angle from 140.7º to 180º. In the phenyl (Ph) containing analogues,[19] the difference in the CNC bond angle increases by a smaller amount (~10º) from 135.2º in PhNCO to 145.1º in PhNCS which is related to a change in the hybridization at nitrogen from a ~$sp^{1.6}$- to a ~sp-hybridized orbital in these two compounds, respectively. Exploring related pairs of compounds with different R groups will provide greater insight into the role of the R substituent and terminal chalcogen on the electronic structures of NCO/NCS-containing species.

Herein, a detailed investigation of the conformational landscape of allyl-NCS is reported through a combination of Fourier transform microwave (FTMW) spectroscopy in a supersonic jet expansion and quantum mechanical calculations. Guided by the construction of potential energy surfaces that account for dispersive interactions, transitions due to two distinct conformers were observed in the rotational spectrum. This includes the first assignment of the new global minimum geometry, conformer I. In addition to hyperfine structure due to the ^{14}N quadrupole nucleus, transitions from minor isotopologues of all heavy atoms (^{13}C, ^{15}N and ^{34}S) were observed in natural abundance for conformer I allowing experimental geometries to be derived. Differences in the conformational equilibrium of allyl-NCO and allyl-NCS are discussed as are changes in the geometry of conformer I by comparing the derived potential energy surfaces and results from natural bond orbital analyses.

3.3 Experimental Methods

The rotational spectrum of allyl-NCS (Sigma-Aldrich, 94%, bp: 150°C) was collected using a chirped pulse (cp) and a Balle-Flygare Fourier transform microwave (FTMW) spectrometer, both of which have been described previously.[20,21] Briefly, a gas mixture was prepared containing ~1% allyl-NCS in neon buffer gas and delivered to the high vacuum chamber through a pulsed nozzle. The resulting supersonic jet expansion cools the sample to a rotational temperature of ~5 K thereby favoring low energy conformations. Initially, a broadband spectrum was recorded from 8-18 GHz in segments of 2 GHz using the cp-FTMW spectrometer. Rotational transitions belonging to the parent species of two conformers, later determined to be conformers I and III (see Computational Methods below), were assigned in addition to those of their minor heavy isotopologues (^{13}C, ^{15}N, and ^{34}S) in natural abundance. A 3 GHz portion of the cp-FTMW

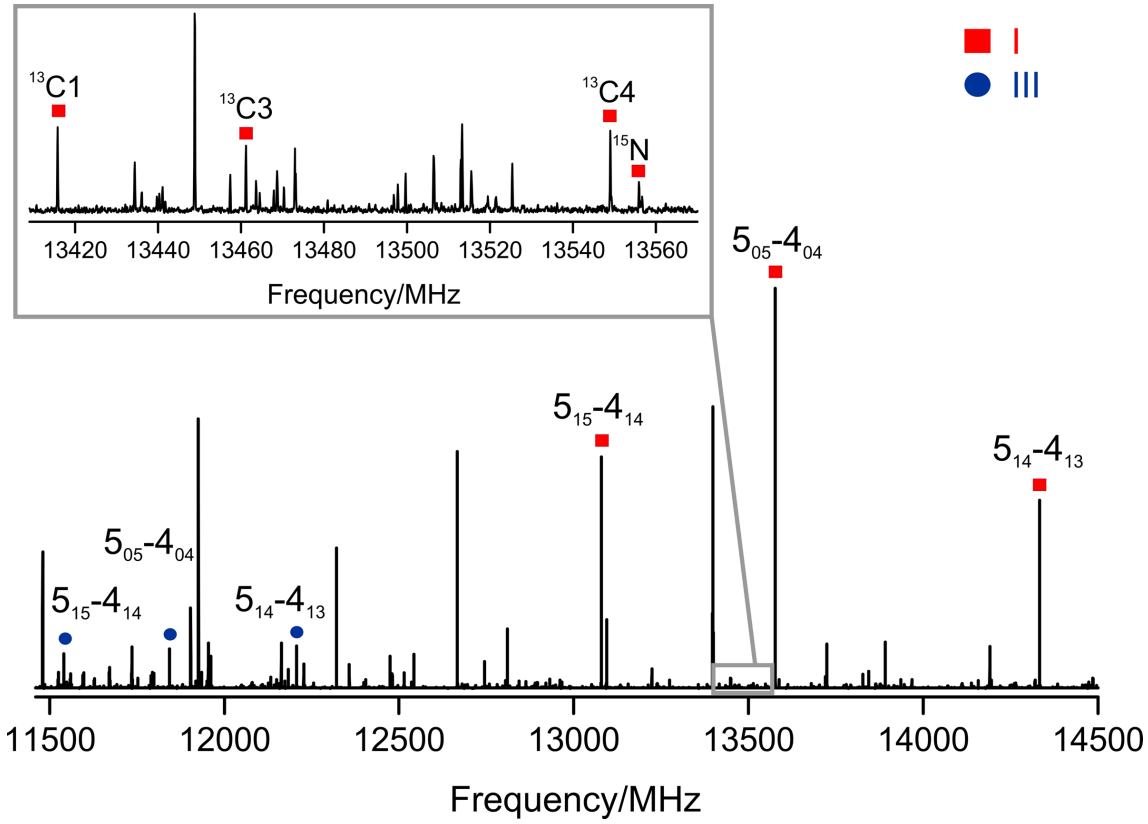

Fig. 3.2 Sample 3 GHz segment of the cp-FTMW spectrum. The 5_{05}-4_{04} rotational transitions due to ^{13}C and ^{15}N species of conformer I are shown in the enhanced portion of the spectrum. (3 million FIDs).

spectrum is shown in Fig. 2. Following initial assignment of the survey spectrum, final measurements were done using the Balle-Flygare FTMW spectrometer from 4-26 GHz in order to resolve the hyperfine structure due to the presence of the ^{14}N nucleus as well as lower intensity transitions that were not observed in the cp-FTMW data. A sample transition recorded using the cavity-based FTMW instrument is shown in Fig. 3. Transitions recorded using this higher resolution spectrometer appear as doublets due to the Doppler effect as a result of the collinear nature of the resonator axis and the jet expansion. Individual components have line widths of approximately 7 kHz (FWHM) and the line positions are determined to roughly ±2 kHz.

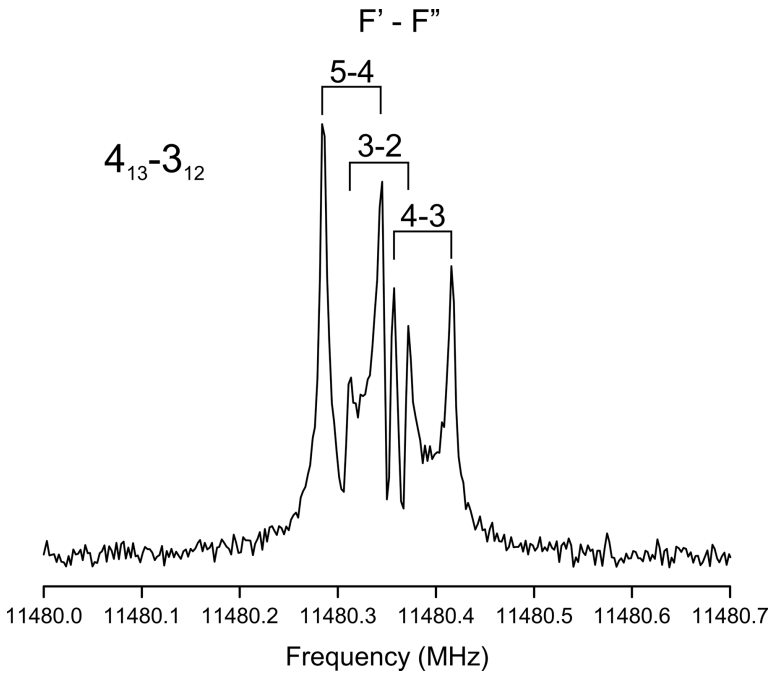

Fig. 3.3 Sample Balle-Flygare FTMW spectrum (410 cycles) showing the 4_{13}-3_{12} rotational transition of conformer I including the ^{14}N hyperfine structure.

3.4 Computational Methods

The energy minima of allyl-NCS were first identified through the construction of three-dimensional potential energy surfaces (PES) created by scanning both the dihedral angles δ and θ in 36 steps of 10° while allowing all other parameters to relax. These scans were conducted using density functional theory (DFT) and second order Møller-Plesset perturbation theory (MP2)[22] calculations with the Gaussian 16 Revision B.01 software.[23] For the DFT calculations, we tested the popular B3LYP[24,25] method along with its B3LYP-D3(0) and B3LYP-D3(BJ) versions, which include Grimme's dispersion corrections with the zero-damping and Becke-Johnson damping schemes,[26,27] respectively. All initial calculations were carried out using the cc-pVTZ basis set.[28–30] The PES obtained are shown in Fig. 4. In the end, five energy minima, which resemble the ones reported for allyl-NCO,[11] were identified from the PES scans and were then fully optimized using

both B3LYP-D3(BJ) and MP2 methods with the cc-pVTZ and cc-pVQZ basis sets. To verify the nature of the stationary points and to compute the electronic energies with zero-point energy (ZPE) corrections, harmonic frequency calculations were also carried out for these minima at the same levels of theory. The optimized geometries corresponding to the five minima are depicted in Fig. 5 while their calculated relative energies, rotational constants and dipole moments calculated using the cc-pVQZ basis set are shown in Table 1.

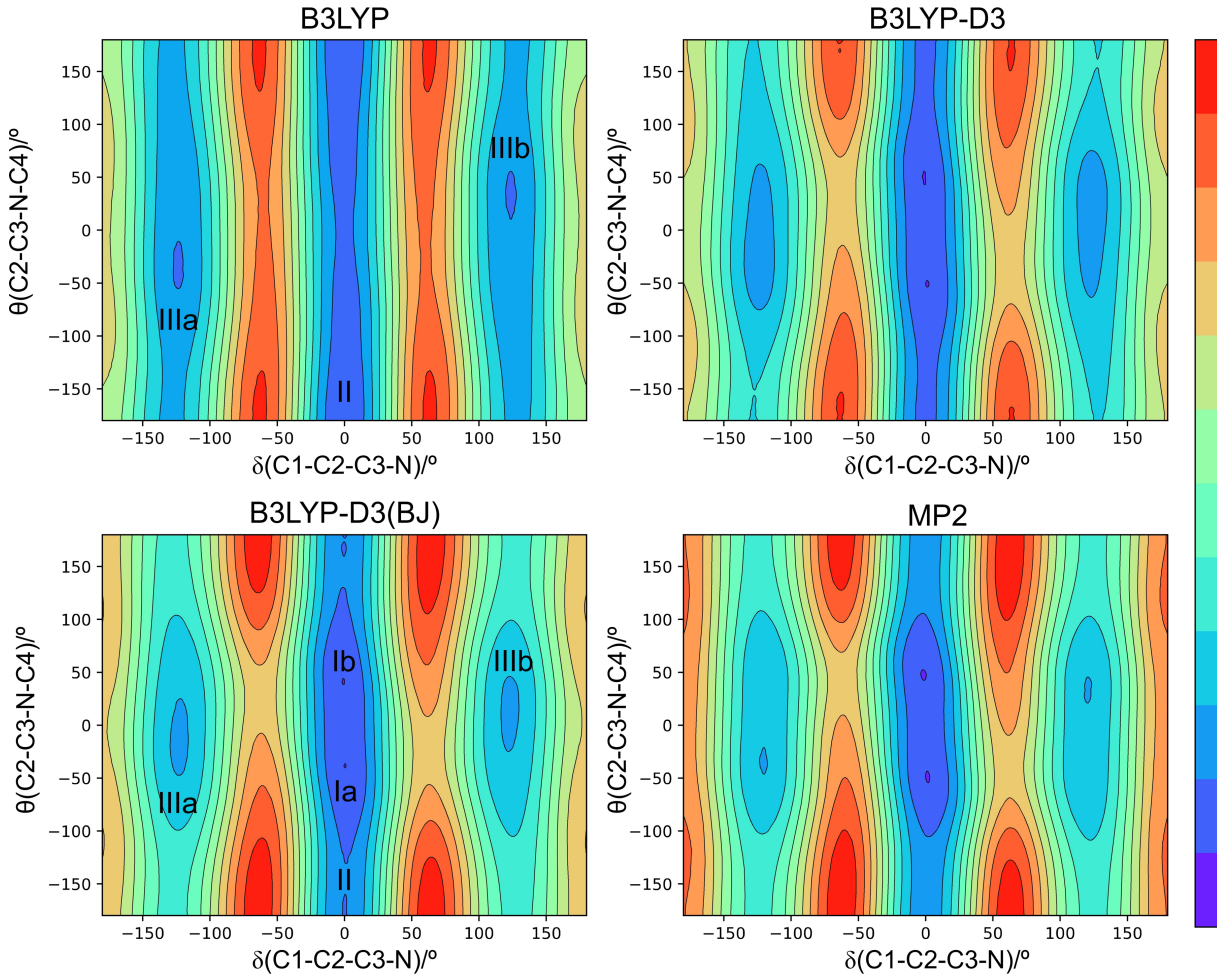

Fig. 3.4 Three-dimensional potential energy surfaces of allyl-NCS obtained by scanning the dihedral angles δ and θ at the B3LYP, B3LYP-D3, B3LYP-D3(BJ) and MP2 methods with the cc-pVTZ basis set. The relative energies are plotted in units of kJ mol^{-1}.

In Fig. 5, the conformers are labeled using Roman numerals from I to III to represent their order of stability with I being the lowest energy geometry. It is worth mentioning that conformers II and III correspond to the *cis* and *gauche* conformers, respectively, previously reported in the literature.[14] As conformers Ia/Ib and IIIa/IIIb are pairs of enantiomers, they present the same rotational and energetic parameters and thus, they are not distinguished in Table 1.

For B3LYP-D3(BJ) calculations, we also tested the performance of different basis sets from the Dunning's family in reproducing the experimental rotational constants for conformer I, detected here for the first time, and the results are summarized in Table S1. The basis sets (cc-

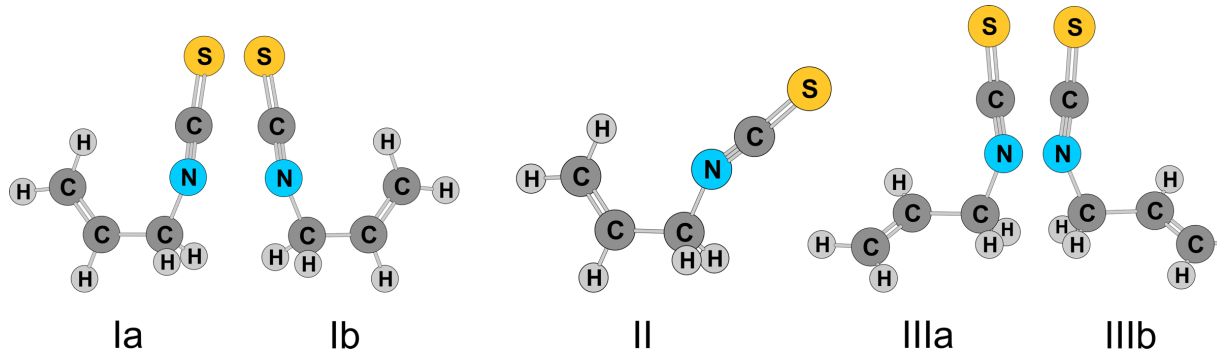

Fig. 3.5 Five optimized geometries corresponding to energy minima of allyl-NCS obtained at the B3LYP-D3(BJ)/cc-pVQZ level of theory. These geometries correspond to conformers Ia/Ib (δ = 0.9°/-0.9, θ = -43.2°/43.2°), II (δ = -0.3°, θ = 180.0°) and IIIa/IIIb (δ = -122.9°/122.9°, θ = -16.9°/16.9°). The Cartesian coordinates for all conformers are provided in Tables S1-S3 in the supporting information (SI) file.

pVXZ, cc-pV(X+d)Z, aug-cc-pVXZ, aug-cc-pV(X+d)Z where X= D, T, Q) chosen vary from double- to quadrupole-zeta and include those with and without additional polarization functions to describe the larger sulfur atom and diffuse functions to account for weak dispersive interactions. Surprisingly, with the exception of the double-zeta basis sets, no significant variations were observed among the results obtained with the triple- and quadrupole-zeta basis sets which

Table 3.1 Calculated Relative Energies, Relative Populations, Equilibrium Rotational Constants and Dipole Moment Components for the Conformers of Allyl Isothiocyanate.

Constants	I		II		III	
	B3LYP-D3(BJ)	MP2	B3LYP-D3(BJ)	MP2	B3LYP-D3(BJ)	MP2
ΔE^a/kJ mol^{-1}	0.0	0.0	1.6	2.4	2.6	3.4
$P_{\Delta E}{}^b$/%	53.4	61.0	28.0	23.1	18.6	15.9
$\Delta E_{ZPE}{}^c$/ kJ mol^{-1}	0.0	0.0	1.0	1.7	2.5	3.3
$P_{\Delta EZPE}{}^d$/%	49.1	56.8	32.9	28.0	18.0	15.2
A/MHz	7018	7052	12176	11799	8373	8816
B	1488	1505	1121	1138	1229	1210
C	1245	1260	1033	1045	1108	1101
P_{aa} /amu Å^2	337	333	449	442	404	410
P_{bb}	69.2	68.5	40.0	41.2	52.6	49.3
P_{cc}	2.86	3.19	1.55	1.66	7.73	7.99
$\|\mu_a\|$/D	3.3	3.3	2.9	3.0	3.3	3.3
$\|\mu_b\|$	0.7	0.7	1.4	1.3	0.5	0.5
$\|\mu_c\|$	0.3	0.4	0.0	0.1	0.3	0.4

[a]Electronic energy relative to the most stable conformer I; [b]Relative population at 298K based on the electronic energies; [c]Electronic energy with zero-point energy (ZPE) corrections relative to the most stable conformer I; [d]Relative population at 298K based on the electronic energies with ZPE corrections.

reproduced the experimental rotational constants to within 0.7%. Similar results were observed in the benchmark study of allyl-NCO.[11]

Given the possibility of conformational changes during supersonic jet expansion, interconversion pathways were also calculated by scanning either the δ or θ dihedral angle in 36 steps of 10° at the B3LYP-D3(BJ)/cc-pVQZ level of theory for comparison with those of allyl-NCO.[11] During the scans, all other geometric parameters were allowed to relax. The calculated relaxation pathways are shown in Fig. 6. To obtain more accurate barriers for the interconversion of conformers along these pathways, the transition state points located on the PES were fully optimized at the B3LYP-D3BJ/cc-pVQZ level. Frequency calculations within the harmonic approximation at the same level of theory confirm the nature of the transition state geometries which exhibit one imaginary frequency. Finally, to examine differences in the electronic

environment of allyl-NCS and allyl-NCO, natural bond orbital (NBO) calculations were done for both molecules at the B3LYP-D3(BJ)/cc-pVTZ level using the NBO 6.0 program.[31]

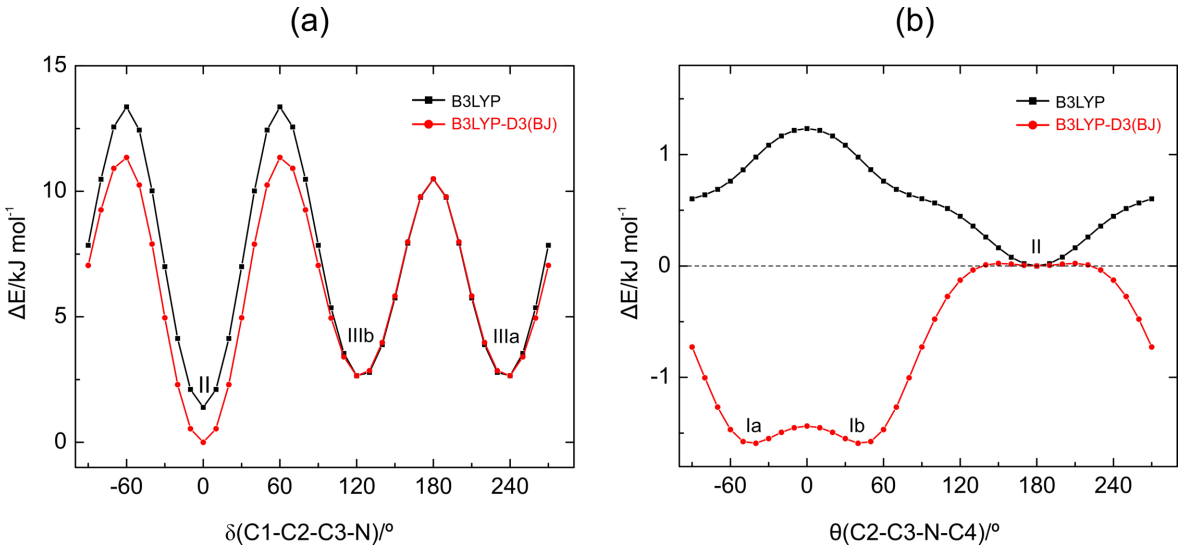

Fig. 3.6 a) Relaxation pathway calculated as a result of scanning the dihedral angle δ in 36 steps of 10º at the B3LYP/cc-pVQZ and B3LYP-D3(BJ)/cc-pVQZ levels of theory. b) Relaxation pathway calculated when scanning the dihedral angle θ in 36 steps of 10º, where the initial value of δ is 0º, at B3LYP/cc-pVQZ and B3LYP-D3(BJ)/cc-pVQZ levels of theory.

3.5 Spectral Analysis

Two sets of R-branch *a*- and *b*-type rotational transitions belonging to two different species with sizeable $|\mu_a|$ and $|\mu_b|$ permanent electric dipole moment components were assigned in the rotational spectrum of allyl-NCS. By comparing the experimental rotational constants with those predicted in Table 1, the transitions were attributed to the parent species of conformers I and III. In total, 96 (79 *a*- and 17 *b*-type) and 68 (53 *a*- and 15 *b*-type) hyperfine components were measured for conformers I and III, respectively. Despite accurate frequency predictions, no *c*-type transitions were observed which is consistent with the smaller values of $|\mu_c|$ (Table 1). For both conformers, transitions corresponding to the singly substituted ^{34}S isotopologue in natural

abundance were assigned and as the spectral features of conformer I dominate the spectrum in Fig. 2, there was sufficient intensity to assign transitions due to its ^{13}C and ^{15}N isotopologues. The measured transitions for each species were fit with Pickett's SPFIT program[32] using Watson's S-reduced Hamiltonian in the I^r representation.[33] During the spectral analysis, the parameters that were not well-determined were fixed to either the calculated values or to the corresponding parent values. The resulting spectroscopic constants are shown in Tables 2 and 3 while the lists of observed transitions are shown in Tables S2-S10 in the SI.

Following the determination of accurate rotational constants in Table 2 for the isotopologues of conformer I, the experimental geometry of its heavy atom framework was derived using Kisiel's STRFIT program[34] to fit the effective moments of inertia to a set of geometric parameters. This procedure was carried out by fixing the equilibrium positions of hydrogen atoms to those derived at the B3LYP-D3(BJ)/cc-pVQZ level of theory. The derived r_0 structure successfully reproduced the 21 experimental rotational constants of conformer I of allyl-NCS to within 0.011%. The heavy atom internal coordinates are summarized in Table 4 along with those of conformer I of allyl-NCO.[11] The corresponding parameters for the substitution structure (r_s) based on Kraitchman's equations[35] including Costain errors[36] as implemented in Kisiel's KRA program,[34] equilibrium geometry (r_e) and transition state (r_{ts}) for the interconversion between the conformer pair (Ia/Ib) are also provided. For the r_s structure, the c-coordinate of C1 was set to zero as the Kraitchman equations yielded an imaginary number due to its proximity to the ab-plane and signs of the coordinates were inferred from the r_e structure. The principal atomic coordinates for all four geometries (r_e, r_{ts}, r_0 and r_s) are available in the accompanying SI.

Table 3.2 Ground State Spectroscopic Constants Obtained for the Parent, ^{34}S, ^{13}C and ^{15}N Species of Conformer I.

	B3LYP-D3(BJ)[a]	Parent	^{34}S	$^{13}C1$	$^{13}C2$	$^{13}C3$	$^{13}C4$	^{15}N
Rotational Constants /MHz								
A	7018.38	6974.18615(71)	6958.4085(10)	6778.019(16)	6967.775(28)	6869.616(27)	6959.964(16)	6888.2007(91)
B	1488.33	1500.19662(12)	1456.87719(27)	1485.94460(26)	1476.20010(41)	1488.88154(36)	1497.20146(21)	1499.98257(13)
C	1245.07	1248.49890(11)	1217.88160(23)	1232.27174(25)	1231.70608(36)	1237.31331(31)	1245.99526(21)	1245.80534(13)
Centrifugal Distortion Constants /kHz								
D_J	1.12	1.05815(66)	0.9960(19)	1.0745(14)	1.0280(20)	1.0110(27)	1.0550(12)	1.04974(77)
D_{JK}	-4.43	-3.3149(53)	-3.124(10)	-3.630(10)	-3.598(29)	-2.440(16)	-3.4702(80)	-3.4799(47)
D_K	49.06	[49.06][b]	[49.06][b]	[49.06][b]	[49.06][b]	[49.06][b]	[49.06][b]	[49.06][b]
d_1	-0.35	-0.32019(90)	-0.2957(27)	-0.3260(23)	-0.3057(44)	-0.3090(38)	-0.3176(18)	-0.3208(11)
d_2	-0.04	-0.03868(48)	[-0.0387][c]	[-0.0387][c]	[-0.0387][c]	[-0.0387][c]	[-0.0387][c]	[-0.0387][c]
^{14}N Quadrupole Coupling Constants /MHz								
$3/2\ \chi_{aa}$	2.82	2.7147(21)	2.7292(78)	2.6999(60)	2.710(11)	2.7490(92)	2.7087(44)	-
$1/4\ (\chi_{bb}-\chi_{cc})$	-0.03	-0.03094(79)	[-0.0309][c]	[-0.0309][c]	[-0.0309][c]	[-0.0309][c]	[-0.0309][c]	-
rms /kHz	-	1.4	1.5	1.4	1.7	1.5	1.4	0.5
# lines	-	97	49	43	42	36	59	22

[a]Dunning's cc-pVQZ basis set used. [b]Value fixed that from the quantum chemical calculation. [c]Value fixed to that derived for the parent isotopologue.

Table 3.3 Ground State Spectroscopic Constants Obtained for the Parent and ^{34}S Species of Conformer III.

	B3LYP-D3(BJ)[a]	Parent	^{34}S
Rotational Constants /MHz			
A	8372.97	8045.40393(50)	8011.01(22)
B	1228.71	1254.99398(11)	1221.74385(33)
C	1107.68	1121.603769(98)	1094.11081(40)
Centrifugal Distortion Constants /kHz			
D_J	2.20	2.10210(87)	2.1062(31)
D_{JK}	-78.53	-63.831(12)	-64.225(29)
D_K	908.24	[908.24][b]	[908.24][b]
d_1	-0.55	-0.52318(89)	-0.3965(32)
d_2	-0.01	-0.01443(63)	[-0.0144][c]
^{14}N Quadrupole Coupling Constants /MHz			
3/2 χ_{aa}	2.92	2.7908(32)	2.825(35)
1/4 (χ_{bb}-χ_{cc})	-0.12	-0.1037(11)	[-0.104][c]
rms /kHz	-	1.5	1.6
no. lines	-	68	24

[a]Dunning's cc-pVQZ basis set used. [b]Value fixed that from the quantum chemical calculation. [c]Value fixed to that derived for the parent isotopologue.

Table 3.4 Comparison of the Equilibrium (r_e) (B3LYP-D3(BJ)/cc-pVQZ)[a] and Effective Ground State (r_0) Geometries for Conformer I of Allyl-NCS and Allyl-NCO and Transition State Geometry (r_{ts}) for Ia/Ib Interconversion of Allyl-NCS (B3LYP-D3(BJ)/cc-pVQZ

	Allyl-NCS				Allyl-NCO[b]	
	r_e[b]	r_s	r_0	r_{ts}	r_e[b]	r_0
C_2-C_1	1.323	1.347(7)	1.339(5)	1.322	1.323	1.341(11)
C_3-C_2	1.504	1.495(6)	1.504(5)	1.504	1.502	1.498(10)
N-C_3	1.424	1.529(16)	1.429(7)	1.420	1.438	1.453(22)
C_4-N	1.184	1.081(14)	1.178(7)	1.181	1.197	1.189(14)
S/O-C_4	1.583	1.594(4)	1.583(4)	1.585	1.170	1.171(13)
∠ C_3-C_2-C_1	126.4	125.6(3)	125.8(2)	126.6	126.6	125.8(3)
∠ N-C_3-C_2	114.8	115.3(3)	114.5(3)	115.2	115.2	115.1(5)
∠ C_4-N-C_3	150.7	148.9(11)	152.6(3)	154.3	138.8	137.5(4)
∠ S/O-C_4-N	176.1	173.0(14)	[176.1][c]	176.3	173.4	[173.4][c]
τ N-C_3-C_2-C_1	0.86	-1.3(39)	[0.86][c]	0.0	0.4	[0.4][c]
τ C_4-N-C_3-C_2	-43.2	-32(5)	-33.9(4)	0.0	-58.9	-57.8(8)
τ S/O-C_4-N-C_3	178.6	178(17)	[178.6][c]	180.0	179.9	[179.9][c]

[a]Dihedral angles consistent with Ia enantiomer; [b]Reference 11; [c]Parameters held fixed to equilibrium values.

3.6 Discussion

The exploration of the conformational landscape of allyl-NCS through the construction of three-dimensional PES led to the identification of five energy minima reported in Fig. 5. By comparing the PES obtained at the different levels (Fig. 4), one can see that standard B3LYP calculations fail to identify conformer I as an energy minimum, while the dispersion-corrected DFT and MP2 methods find all three conformers of allyl-NCS. The absence of conformer I in the B3LYP PES is related to the inability of this computational method to describe the attractive dispersive π⋯π interaction between the thiocyanato (-N=C=S) and the allyl (-CH=CH_2) group. The importance of dispersion corrections in obtaining an accurate picture of the conformer landscape has been reported for other systems including those with only first row elements such

as methyl jasmonate and zingerone.[37] Similar results were observed in the benchmark study of the PES of the isovalent allyl-NCO compound, where among more than 20 functionals tested, dispersion uncorrected DFT methods failed to describe the proper conformational distribution.[11] Thus, although allyl-NCS was investigated previously using both computational[16,38] and experimental[14,15,16] methods, the present work is the first study to predict and confirm the presence of conformer I, the lowest energy conformation.

From the intensities of the observed transitions in Fig. 1 and considering that conformers I and III are predicted to have similar $|\mu_a|$ and $|\mu_b|$ values (Table 1), conformer I is the dominant species in the spectrum. Based on the calculated populations at 298K (Table 1), conformer II is predicted to be more stable than III but no transitions attributable to this geometry were assigned. It has been shown empirically that in a cold rare gas jet, higher energy conformers undergo relaxation to lower energy forms when the interconversion barrier is lower than ~4.8 kJ/mol.[39] This empirical rule of thumb has been used to justify the absence of conformers in other systems with alkane backbones such as perillyl alcohol where eight of 12 low energy conformers persisted in the jet.[40] By analyzing the relaxation pathway from II→I for allyl-NCS (Fig. 6b) the calculated interconversion barrier is only ~0.02 kJ/mol (0.05 kJ/mol with ZPE corrections)(B3LYP-D3(BJ)/cc-pVQZ) which implies that conformer II will relax to conformer I in the expansion. For comparison, the barrier is smaller than that reported for allyl-NCO (0.13 kJ/mol with ZPE) at the same level of theory which was used to justify the lack of features arising from conformer II in its microwave spectrum.[11] Such a flat PES along the δ=0 coordinate calls into question whether the ZPE corrections, based on harmonic vibrations, are valid but nevertheless, conformer II was a true minimum on the PES of allyl-NCS tested at the B3LYP-D3(BJ) (cc-pVQZ, aug-cc-pVTZ, aug-cc-pVQZ) and MP2 (cc-pVQZ, aug-cc-pVTZ) levels based on the absence of imaginary frequencies.

The fact that conformer II was not observed in a static gas sample[14,15] certainly calls into question whether this is a stable conformer.

Although conformers I and III exist as pairs of enantiomers (Ia/Ib and IIIa/IIIb) which are equivalent minima on the PES, no tunnelling splitting related to their interconversion was observed. This was surprising initially as a tunnelling splitting was reported for the transitions of conformer I in allyl-NCO.[11] To understand this, the heights of the energy barriers associated with the interconversion between the enantiomer pairs of I and III were evaluated from the potential energy curves in Fig. 6. The barrier between Ia and Ib (Fig. 6b) is calculated to be ~0.15 kJ/mol, but when accounting for ZPE corrections, the energy difference between conformer I and the transition state is lowered to -0.17 kJ/mol. This indicates that the interconversion between Ia and Ib is barrierless in allyl-NCS and is consistent with the observed spectra in which *c*-type transitions are not observed. For comparison, in allyl-NCO,[11] the ZPE-corrected interconversion barrier in conformer I is higher (~0.8 kJ/mol) which supports the observation of tunnelling splitting. Conversely, for conformer III of allyl-NCS, the relatively high energy barrier between IIIa and IIIb (Fig. 6a) of 7.88 kJ/mol is expected to quench tunnelling and this barrier is comparable to that reported for conformer III of allyl-NCO (7.86 kJ/mol).[11]

To better rationalize why the enantiomeric interconversion barrier is larger by ~1 kJ/mol for conformer I of allyl-NCO compared with that of allyl-NCS (while those of conformers III are nearly identical before ZPE correction), we investigated the potential energy curves for the Ia/Ib tunnelling pathway for allyl-NCS in Fig. 6b with the analogous profile for allyl-NCO in reference 11. By analyzing the B3LYP energy (without the inclusion of dispersive corrections), one can see that the transition state structure (C-C-N-C= 0º) of allyl-NCO already lies ~1 kJ/mol higher in energy than that of allyl-NCS (when referenced to conformer II in each case). From the geometry

of the transition states as shown in Fig. S1 of the SI, we assert that this higher barrier is related to steric repulsion as the allyl and isocyanato groups are in closer proximity in allyl-NCO. When dispersion corrections are included, the Ia/Ib interconversion barrier is retained in allyl-NCO but the motion is barrierless in allyl-NCS.

The substitution (r_s) and effective ground state (r_0) geometries of conformer I in Table 4 are in good agreement within the derived uncertainties of each method with the precision of the former limited by relatively large Costain errors in the coordinates of atoms close to inertial axes. The Costain errors are meant to account for vibrational effects[36] and the resulting uncertainties in the r_s parameters, particularly the dihedral angles, is consistent with the influence of a large amplitude motion such as that required for interconversion of the Ia/Ib enantiomer pair as seen in Figure 6. Thus, it is evident that the experimental rotational constants used to derive the r_s and r_0 geometries involve contributions from this barrierless motion and should be interpreted with caution. It is worth noting that comparison of the r_0, equilibrium (r_e) and transition state (r_{ts}) geometries in Table 4 reveals that most parameters actually match to within 2σ. The largest discrepancy is found in the dihedral angle τ(C4-N-C3-C2) (θ) that corresponds to this large amplitude motion with the value obtained from experiment (-33.9(4)°) (where the negative sign refers to conformer Ia) falling between those calculated for the global minimum (-43.2°) and the transition state (0°). This occurs because the effective ground state rotational constants used to derive the experimental geometries are expectation values that depend on the squares of distances through the moments of inertia such that the contributions from the positive and negative motions along θ do not cancel. A similar explanation was invoked to rationalize the spectrum of 2-fluoroethanol···H_2O as arising from an intermediate geometry of two low-lying conformers (I and II) that interconvert.[41] Furthermore, for allyl-NCS, the r_s geometry provides a second estimate of

the θ dihedral angle (-32(5)°) that is independent of *a priori* assumptions from quantum chemical calculations (beyond the signs of the individual coordinates). One can more directly observe the effects of large amplitude motions over θ for conformer I of allyl-NCS through investigation of the planar moments. Using the rotational constants for the parent isotopologue of conformer I from Table 2, P_{cc} is 2.28 amu Å^2 which falls between the B3LYP-D3(BJ)/cc-pVQZ estimated values for the equilibrium structure (2.86 amu Å^2) (Table 1) and the heavy atom planar transition state (1.53 amu Å^2). Interestingly, the latter is nearly identical to that of the lowest energy conformer of allyl-NC (1.50 amu Å^2)[42] with a backbone similar to that of allyl-NCS conformer II (1.55 amu Å^2) which suggests that this value describes the out-of-plane contributions from the methylene H atoms.

As noted above, beyond the θ coordinate that interconverts the conformer Ia/Ib pair, the remaining geometric parameters in Table 4 for allyl-NCS are strikingly similar which affords the opportunity to look for structural trends among related molecules. Comparison of the r_0 structures of allyl-NCS and allyl-NCO in Table 4 shows that the nature of the chalcogen atom does not significantly alter the geometry of the allyl segment of the molecule despite the fact that conformer I is stabilized by an interaction between the allyl and iso(thio)cyanato fragments. This is consistent with the previously reported geometries of phenyl-NCO and phenyl-NCS which found no differences in the electronic structure of the ring backbone despite the possibility of a change in π-delocalization of the ring with added -NCO or -NCS substituents.[19] The terminal chalcogen atom does, however, influence the geometry around nitrogen as observed from the ~15° increase in the C_4-N-C_3 bond angle upon replacing oxygen with sulfur. The increased angle around nitrogen in allyl-NCS is accompanied by a decrease in the C4-N and N-C3 r_e bond lengths. Similar structural changes are observed in other R-NCO and R-NCS species with the R=allyl results in this work

being most similar to those reported for R=cyano in which the C-N-C angle increases by 14° in NCNCS[43] relative to the value in NCNCO.[44] The effect is larger than that reported for R=phenyl (9.9°),[19] H (8°)[45,46] and R= CH_3 (7.5°).[47]

To better comprehend the underlying reasons for the observed changes in geometry, the electronic environment around nitrogen was investigated using the results from natural bond orbital (NBO) analysis for conformers I of allyl-NCO[11] and allyl-NCS. Comparison of the σ-bonding framework around nitrogen reveals that the hybridization of nitrogen is ~$sp^{1.5}$ in allyl-NCO and more sp-like in allyl-NCS which is consistent with the larger C_4-N-C_3 angle in the latter. This ~sp-hybridization implies that the CN portion of the isothiocyanato fragment has more triple bond character which is confirmed by the presence of two occupied π-bonding orbitals between C4 and N in the NBO results and by the absence of an orbital consistent with lone pair electron character on nitrogen. In the isovalent allyl-NCO analogue, on the other hand, there is an orbital that is best described as a nitrogen lone pair and only one π-bond between C4 and N as one would expect for a fragment that more closely approximates sp^2-like hybridization at nitrogen. The variation in electronic structure around nitrogen in allyl-NCO and allyl-NCS is comparable in nature to the trend reported in Ph-NCO and Ph-NCS,[19] although more pronounced when R=allyl. A careful inspection of the orbitals involving nitrogen in Ph-NCS and allyl-NCS show that in the former, one of the π-bonds (C4-N) is primarily localized on N (85%) and thus more closely resembles lone pair character than its counterpart in allyl-NCS (69%) which is more evenly shared. This subtle difference in the electronic environment surrounding nitrogen manifests in a smaller N-C-N bond angle for Ph-NCS (145.2(2)°) than for allyl-NCS (152.0(3)°).

Finally, the influence of the terminal chalcogen atoms on the electronic structure around nitrogen appears largely driven by the differences in the size and electronegativity of oxygen

versus sulfur. Careful study of the nature of the occupied orbitals in allyl-NCS, for example, reveals that the larger sulfur atom has three lone pairs of electrons and forms a single σ-bond with the adjacent C4. In allyl-NCO,[11] in contrast, a π-bond is also formed between the more similarly-sized oxygen and C4 atoms leaving only two lone pairs of electrons on the terminal chalcogen. The NBO results are somewhat surprising, however, as the derived bond lengths for C4-S (1.583(4) Å) and C4-O (1.171(13) Å) in Table 4 are more consistent with typical double bonds C=S (1.60 Å) and C=O (1.20 Å) in these fragments.

3.7 Conclusion

In summary, the conformational landscape of allyl-NCS was examined FTMW spectroscopy in concert with dispersion-corrected DFT and *ab initio* quantum chemical methods. When dispersion interactions are accounted for, a new global minimum is predicted and this new conformer I was observed experimentally for the first time in this work. This reinforces the importance of including dispersion effects when studying conformational space.[37] The geometry of conformer I derived from the experimental rotational constants is consistent with the accompanying potential energy landscape that permits conformer I to undergo large amplitude motions in the θ coordinate to interconvert the enantiomeric pair Ia/Ib. Upon comparison of the geometry of conformer I with that of allyl-NCO, the largest difference observed is the increase in the C-N-C angle in changing the terminal chalcogen atom from oxygen to sulfur. This is explained via the accompanying NBO results which reveal that the hybridization of nitrogen is more ~sp in nature in allyl-NCS compared with ~$sp^{1.5}$ in allyl-NCO.[11] This is consistent with differences in bonding stemming from the disparate sizes and electronegativities of the terminal chalcogen atoms. The differences in the geometry around nitrogen are more pronounced in the allyl-substituted species than those reported for other R-NCO and R-NCS pairs where R=phenyl,[19]

methyl[47] and H.[45,46] This confirms that the orbital character of the adjacent organic fragment is also a key factor that influences the electronic environment at the nitrogen link in this class of molecules.

References

(1) Snyder, L. E.; Buhl; D. Interstellar Methylacetylene and Isocyanic Acid. *Nat. Phys. Sci.* **1973**, *243* (125), 45–46.

(2) Frerking, M. A.; Linke, R. A.; Thaddeus, P. Interstellar Isothiocyanic Acid. *Astrophys. J.* **1979**, *234*, L143–L145.

(3) Brünken, S.; Belloche, A.; Martín, S.; Verheyen, L.; Menten, K. M. Interstellar HOCN in the Galactic Center Region. *Astron. Astrophys.* **2010**, *516* (22), 1–8.

(4) Brünken, S.; Gottlieb, C. A.; McCarthy, M. C.; Thaddeus, P. Laboratory Detection of HOCN and Tentative Identification in Sgr B2. *Astrophys. J.* **2009**, *697* (1), 880–885.

(5) Brünken, S.; Yu, Z.; Gottlieb, C. A.; McCarthy, M. C.; Thaddeus, P. Laboratory Detection of Thiocyanic Acid HSCN. *Astrophys. J.* **2009**, *706* (2), 1588–1593.

(6) Halfen, D. T.; Ziurys, L. M.; Brünken, S.; Gottlieb, C. A.; McCarthy, M. C.; Thaddeus, P. Detection of a New Interstellar Molecule: Thiocyanic Acid HSCN. *Astrophys. J.* **2009**, *702* (2), L124–L127.

(7) Halfen, D. T.; Ilyushin, V. V.; Ziurys, L. M. Interstellar Detection of Methyl Isocyanate CH3NCO in Sgr B2(N): A Link From Molecular Clouds to Comets. *Astrophys. J. Lett.* **2015**, *812*, L5.

(8) Cernicharo, J.; Kisiel, Z.; Tercero, B.; Kolesniková, L.; Medvedev, I. R.; López, A.; Fortman, S.; Winnewisser, M.; de Lucia, F. C.; Alonso, J. L.; et al. A Rigorous Detection of Interstellar CH 3 NCO: An Important Missing Species in Astrochemical Networks. *Astron. Astrophys.* **2016**, *587*, L4.

(9) Zhang, Y. Cancer-Preventive Isothiocyanates: Measurement of Human Exposure and Mechanism of Action. *Mutat. Res-Fund. Mol. M.* **2004**, *555* (1–2), 173–190.

(10) Lin, C.-Mi.; Preston, J. F.; Wei, C.-I. Antibacterial Mechanism of Allyl Isothiocyanate. *J. Food. Prot.* **2000**, *63* (6), 727–734.

(11) Sun, W.; Sogeke, O. P.; Silva, W. G. D. P.; van Wijngaarden, J. Dispersion-Driven Conformational Preference in the Gas Phase: Microwave Spectroscopic and Theoretical Study of Allyl Isocyanate. *J. Chem. Phys.* **2019**, *151* (19), 194304.

(12) Maiti, S.; Jaman, A. I.; Nandi, R. N. Microwave Spectrum of Allyl Isocyanate: Gauche Conformer. *J. Mol. Spectrosc.* **1993**, *158* (1), 8–13.

(13) Jaman, A. I.; Bangal, P. R. Millimeter-Wave Spectrum and Ab Initio DFT Calculation of the C-Gauche Conformer of Allyl Isocyanate. *J. Mol. Spectrosc.* **2009**, *255* (2), 134–138.

(14) Maiti, S.; Jaman, A. I.; Nandi, R. N. Microwave Spectrum of Allyl Isothiocyanate: Gauche Conformer. *J. Mol. Spectrosc.* **1994**, *165* (1), 168–172.

(15) Jaman, A. I. Centrifugal Distortion Analysis of the Microwave Spectrum of Allyl Isothiocyanate (C-Gauche Conformer). *PRAMANA-J. Phys.* **1999**, *53* (5), 857–862.

(16) Glaser, R.; Hillebrand, R.; Wycoff, W.; Camasta, C.; Gates, K. S. Near-Silence of Isothiocyanate Carbon in 13C NMR Spectra: A Case Study of Allyl Isothiocyanate. *J. Org. Chem.* **2015**, *80* (9), 4360–4369.

(17) Ross, S. C.; Cooper, T. A.; Firth, S.; Kroto, H. W.; Walton, D. R. M. The Microwave Spectrum and Semirigid Bender Analysis of Isocyanatoethyne, HCCNCO. *J. Mol. Spectrosc.* **1992**, *152*, 152–167.

(18) Sun, W.; Davis, R. L.; Thorwirth, S.; Harding, M. E.; van Wijngaarden, J. A Highly Flexible Molecule: The Peculiar Case of Ethynyl Isothiocyanate HCCNCS. *J. Chem. Phys.* **2018**, *149*, 104304.

(19) Sun, W.; Silva, W. G. D. P.; van Wijngaarden, J. Rotational Spectra and Structures of Phenyl Isocyanate and Phenyl Isothiocyanate. *J. Phys. Chem. A.* **2019**, *123*, 2351–2360.

(20) Sedo, G.; van Wijngaarden, J. Fourier Transform Microwave Spectra of a New Isomer of OCS-CO2. *J. Chem. Phys.* **2009**, *131*, 44303.

(21) Evangelisti, L.; Sedo, G.; van Wijngaarden, J. Rotational Spectrum of 1,1,1-Trifluoro-2-Butanone Using Chirped-Pulse Fourier Transform Microwave Spectroscopy. *J. Phys. Chem. A.* **2011**, *115* (5), 685–690.

(22) Møller, C.; Plesset, M. S. Note on an Approximation Treatment for Many-Electron Systems. *Phys. Rev.* **1934**, *46* (7), 618–622.

(23) Frisch, M. J.; Trucks, G. W.; Schlegel, H. B.; Scuseria, G. E.; Robb, M. A.; Cheeseman, J. R.; Scalmani, G.; Barone, V.; Petersson, G. A.; Nakatsuji, H.; et al. *Gaussian 16*, Revision B.01; Gaussian, Inc.: Wallingford, CT 2016.

(24) Becke, A. D. Density-Functional Exchange-Energy Approximation with Correct Asymptotic Behavior. *Phys. Rev. A* **1988**, *38* (6), 3098–3100.

(25) Lee, C.; Yang, W.; Parr, R. G. Development of the Colle-Salvetti Correlation-Energy Formula into a Functional of the Electron Density. *Phys. Rev. B* **1988**, *37* (2), 785–789.

(26) Grimme, S.; Ehrlich, S.; Goerigk, L. Effect of the Damping Function in Dispersion Corrected Density Functional Theory. *J. Comput. Chem.* **2011**, *32* (7), 1456–1465.

(27) Becke, A. D.; Johnson, E. R. A Density-Functional Model of the Dispersion Interaction. *J. Chem. Phys.* **2005**, *123* (15), 154101.

(28) Dunning, T. H. Gaussian Basis Sets for Use in Correlated Molecular Calculations. V. Core-valence Basis Sets for Boron through Neon. *J. Chem. Phys.* **1989**, *90* (2), 1007–1023.

(29) Kendall, R. A.; Dunning, T. H.; Harrison, R. J. Electron Affinities of the First-row Atoms Revisited. Systematic Basis Sets and Wave Functions. *J. Chem. Phys.* **1992**, *96* (9), 6796–6806.

(30) Woon, D. E.; Dunning, T. H. Gaussian Basis Sets for Use in Correlated Molecular Calculations. III. The Atoms Aluminum through Argon. *J. Chem. Phys.* **1993**, *98* (2), 1358–1371.

(31) Glendening, E. D. .; Badenhoop, J. K. .; Reed, A. E. .; Carpenter, J. E. .; Bohmann, J. A. .; Morales, C. M. .; Landis, C. R. .; Weinhold, F. *NBO* 6.0; Theoretical Chemistry Institute, University of Wisconsin, Madison, WI 2013.

(32) Pickett, H. M. The Fitting and Prediction of Vibration-Rotation Spectra with Spin Interactions. *J. Mol. Spectrosc.* **1991**, *148* (2), 371–377.

(33) Watson, J. K. G. *Vibration Spectra and Structure*: *A Series of Advances*; Durig, J. R.; Ed.; Elsevier: New York, 1977; Vol. *6*, pp 1-89.

(34) Kisiel, Z. PROSPE - Programs for ROtational SPEctroscopy http://www.ifpan.edu.pl/~kisiel/prospe.htm (accessed Feb 3, 2020).

(35) Kraitchman, J. Determination of Molecular Structure from Microwave Spectroscopic Data. *Am. J. Phys.* **1953**, *21* (1), 17–24.

(36) Costain, C. C. *Further Comments on the Accuracy of r_s Substitution Structures*; Bradley, W. F.; Hanson, H. P.; Eds.; Transactions of the American Crystallographic Association: Austin, 1966; Vol. 2, pp 157-163.

(37) Uriarte, I.; Insausti, A.; Cocinero, E. J.; Jabri, A.; Kleiner, I.; Mouhib, H.; Alkorta, I. Competing Dispersive Interactions: From Small Energy Differences to Large Structural Effects in Methyl Jasmonate and Zingerone. *J. Phys. Chem. Lett.* **2018**, *9* (20), 5906–5914.

(38) Chrostowska, A.; Darrigan, C.; Dargelos, A.; Graciaa, A.; Guillemin, J. C. Isoselenocyanates versus Isothiocyanates and Isocyanates. *J. Phys. Chem. A* **2018**, *122* (11), 2894–2905.

(39) Ruoff, R. S.; Klots, T. D.; Emilsson, T.; Gutowsky, H. S. Relaxation of Conformers and Isomers in Seeded Supersonic Jets of Inert Gases. *J. Chem. Phys.* **1990**, *93* (5), 3142–3150.

(40) Xie, F.; Seifert, N. A.; Heger, M.; Thomas, J.; Jäger, W.; Xu, Y. The Rich Conformational Landscape of Perillyl Alcohol Revealed by Broadband Rotational Spectroscopy and Theoretical Modelling. *Phys. Chem. Chem. Phys.* **2019**, *21* (28), 15408–15416.

(41) Huang, W.; Thomas, J.; Jäger, W.; Xu, Y. Tunnelling and Barrier-Less Motions in the 2-Fluoroethanol–Water Complex: A Rotational Spectroscopic and Ab Initio Study. *Phys. Chem. Chem. Phys.* **2017**, *19* (19), 12221–12228.

(42) Haykal, I.; Margulès, L.; Huet, T. R.; Motyienko, R. A.; Écija, P.; Cocinero, E. J.; Basterretxea, F.; Fernández, J. A.; Castaño, F.; Lesarri, A.; et al. The CM-, MM-, and SUB-MM-WAVE Spectrum of Allyl Isocyanide and Radioastronomical Observations in Orion KL and the SgrB2 Line Surveys. *Astrophys. J.* **2013**, *777* (2), 2–9.

(43) King, M. A.; Kroto, H. W.; Landsberg, B. M. Microwave Spectrum of the Quasilinear Molecule, Cyanogen Isothiocyanate (NCNCS). *J. Mol. Spectrosc.* **1985**, *113* (1), 1–20.

(44) Hocking, W. H.; Gerry, M. C. L. The Microwave Spectrum of Cyanogen Isocyanate (NCNCO). *J. Mol. Spectrosc.* **1976**, *59* (3), 338–354.

(45) Hocking, W. H.; Gerry, M. C. L.; Winnewisser, G. The Microwave and Millimetre Wave Spectrum, Molecular Constants, Dipole Moment, and Structure of Isocyanic Acid, HNCO. *Can. J. Phys.* **1975**, *53* (19), 1869–1901.

(46) Beard, C. I.; Dailey, B. P. The Structure and Dipole Moment of Isothiocyanic Acid. *J. Chem. Phys.* **1950**, *18* (11), 1437–1441.

(47) Lett, R. G.; Flygare, W. H. Microwave Spectrum, Barrier to Internal Rotation, 14 N Nuclear Quadrupole Interaction, and Normal-Coordinate Analysis in Methylisocyanate, Methylisothiocyanate, and Methylthiocyanate. *J. Chem. Phys.* **1967**, *47* (11), 4730–4750.

(48) Rodríguez-Guerra Pedregal, J.; Gómez-Orellana, P.; Maréchal, J.-D. ESIgen: Electronic Supporting Information Generator for Computational Chemistry Publications. *J. Chem. Inf. Model.* **2018**, *58* (3), 561–564.

Chapter 4. Microwave Spectroscopic Study of benzyl-NCO with Associated benzyl-NCO and benzyl-NCS Computational Analyses

To examine the impact of the side chain structure on the nitrogen electronic environment, the microwave spectrum of benzyl-NCO was studied and a structural analysis was conducted. The results of the structural analysis were then compared to other isocyanates to determine how the structure around nitrogen is influenced by both large and small changes in the R group. Additionally, a benzyl-NCO computational benchmark was done to investigate which level of theory most accurately modeled the experimentally derived benzyl-NCO PES. The results were then used to construct a benzyl-NCS PES in order to predict the change in the molecular structure as a result of chalcogen substitution for the benzyl group which was then compared to the predicted changes for other R groups. The results from the studies of benzyl-NCO and its sulfur counterpart are discussed in the chapter below.

4.1 Introduction

As discussed in chapter 3, while there are large differences between R = H, methyl, phenyl and allyl, which lead to changes in molecular structure around the nitrogen atom, chalcogen substitution from oxygen to sulfur for the allyl group was seen to increase the CNC bond angle by ~15° which is closely aligned with the ~14° increase observed for the cyanogen analogues.[1,2] Using these results as a starting point, the next step was to consider other side chain structures which also feature a linking CH_2 methylene group, in this case the benzyl group, to see whether this represents a larger trend. To examine the impact of both the side chain and chalcogen substitution, different sets of isocyanates and isothiocyanates should be compared which are structurally similar to one another. For this purpose, the rotational spectrum of benzyl-NCO and benzyl-NCS was desired as the benzyl group structure differs from that of the phenyl group only by the addition of a CH_2

fragment while the benzyl and allyl side chains are structurally different, but both contain methylene groups. A literature search revealed that benzyl-NCO had not been previously studied whereas for benzyl-NCS, only the vibrational spectrum had been previously recorded[3] and therefore, in the first step of addressing this question, the rotational spectrum of benzyl-NCO was collected and analyzed. A structural analysis was then performed to determine the molecular structure of the lowest energy conformer and how that structure relates to phenyl-NCO and allyl-NCO to examine the impact of the methylene carbon on the nitrogen electronic environment. Furthermore, to test the ability of different levels of theory to accurately model the conformational landscape of benzyl-NCO, the lowest energy conformer on the 3D PES was optimized at different levels of theory to obtain sets of calculated spectroscopic constants that could be compared to the corresponding experimental constants. Lastly, as the high boiling point of benzyl-NCS (243.0°C[4]) makes it difficult to put this molecule in the gas phase, rather than attempting to collect the rotational spectrum, the outcome of the benzyl-NCO computational benchmark was used to construct the benzyl-NCS PES for a comparison with benzyl-NCO to obtain a best estimate for the changes due to chalcogen substitution for the benzyl group. Afterwards, a comparison was made with the results of the phenyl[5] and allyl[6] studies to derive how changes in R group structure influence the impact of chalcogen substitution.

4.2 Computational Details

Since the PES of both benzyl-NCO and benzyl-NCS had not been previously modeled, constructing a 3D PES for both molecules was a necessary first step. As Fig. 1.4 indicates, the symmetry of the two molecules is such that the entire PES can be examined simply by scanning the movement of the isocyano (or isothiocyano) group relative to the plane of the benzene ring. Therefore, to reduce computational cost, a 3D PES was created for benzyl-NCO and benzyl-NCS

by calculating the electronic energy while simultaneously scanning the dihedral angle δ in 9 steps of 10° and the dihedral angle θ in 36 steps of 10°. For each molecule, scans were conducted using the hybrid DFT functional B3LYP[7,8] with the inclusion of Grimme's D3 dispersion correction[9] and Becke-Johnson damping[10] (B3LYP-(D3BJ)). Additionally, all scan calculations were done using Dunning's cc-pVTZ basis set.[11–13]

Once minima on the 3D surfaces were identified, optimization + frequency calculations were done to generate rotational, centrifugal distortion and ^{14}N quadrupole coupling constants required for spectral analysis, to compute electronic energies with zero-point energy (ZPE) correction and to verify the nature of the stationary points. For the benzyl-NCO computational benchmark, the optimization + frequency calculations were initially carried out using the B3LYP and B3LYP-D3BJ methods. Other hybrid functionals that were tested include the APFD functional from Austin et al.[14] in which a spherical atom model was used to account for empirical dispersion in addition to Chai and Head-Gordon's ωB97X-D functional[15] which was created by combining their ωB97X functional[16] with dispersion corrections based on Grimme's D2 dispersion model.[17] For the benzyl-NCO computational benchmark, all optimization + frequency calculations were done using Dunning's aug-cc-pVTZ basis set.[11]

Based on the outcome of the benzyl-NCO computational study, the level of theory found to be in closest agreement with the experimental constants was used to perform optimization + frequency calculations on minima from the benzyl-NCS PES. The resulting r_e structures were then used in combination with the benzyl-NCO r_e structures to provide a best estimate of the change in the structure around nitrogen as a result of chalcogen substitution for the benzyl group and how that relates to other side chains. Additionally NBO analysis was conducted at the APFD/aug-cc-pVTZ level for the lowest energy conformer on the benzyl-NCO PES as well as the corresponding

benzyl-NCS geometry with the results then compared to other R groups to examine the impact of different side chains on the nitrogen electronic environment. Lastly, for benzyl-NCO, a NCI analysis was done to explain the energetic favourability of one geometry over another in the conformational equilibrium by the presence of weakly favourable intramolecular interactions.

4.3 Experimental Details

A gas mixture of benzyl-NCO was prepared by passing neon buffer gas at 20 psi through a glass bubbler containing a few mL of liquid benzyl-NCO (98%). The gas mixture was then introduced into the high vacuum chamber of the cp-FTMW spectrometer via a supersonic jet expansion where the broadband rotational spectrum was recorded from 7 to 12.2 GHz and from 13 to 15 GHz. The recorded broadband spectrum was used to perform an initial assignment of rotational transitions. Afterwards, a supersonic jet expansion was used to introduce a second gas mixture that had been prepared under identical conditions into the high vacuum chamber of the FTMW spectrometer where high-resolution spectra were recorded for individual transitions in the range of 4-18 GHz. As discussed in chapter 2, a second collection of the benzyl-NCO rotational spectrum was required to record more precise transition frequencies and to observe the expected ^{14}N hyperfine structure.

4.4 Spectral Analysis

An optimization of the geometries corresponding to minima on the benzyl-NCO PES yielded conformers I and II which are shown in Fig. 4.1 along with the calculated population distribution at 298.15 K and corresponding dipole moment components for each conformer. Overall, 49 transitions (corresponding to 130 hyperfine components) ranging from J values of 3 to 10 were assigned to the parent species of conformer I. This assignment was confirmed by the

assignment of transitions due to ^{13}C minor isotopologues in natural abundance. A full line list for the parent and distinct ^{13}C isotopic species is given in Tables S11-S17.

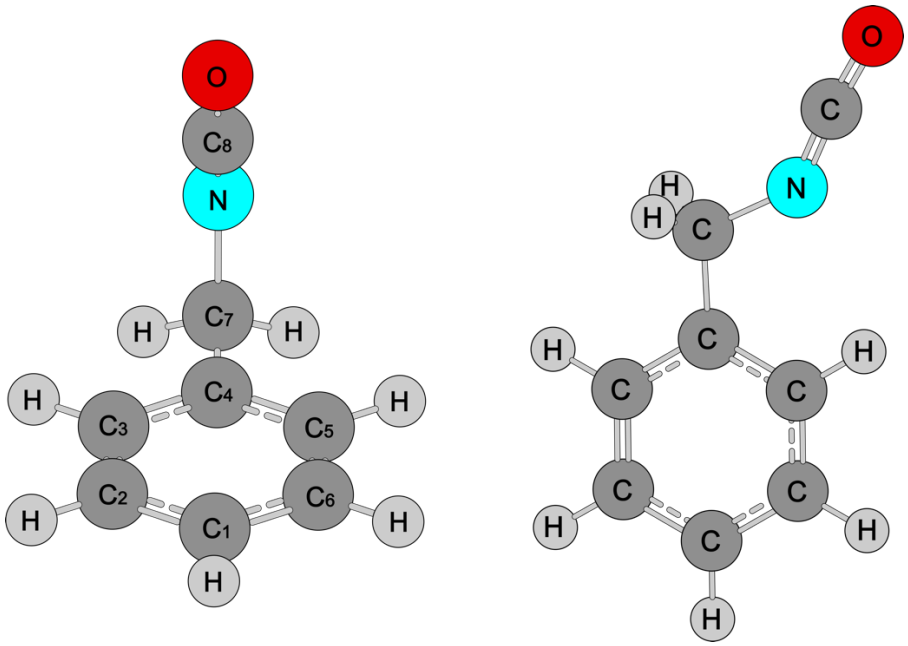

Conformer	I	II
Population (%)[a]	63	37
$\lvert\mu_a\rvert$ (D)	2.2	2.2
$\lvert\mu_b\rvert$ (D)	1.8	1.4
$\lvert\mu_c\rvert$ (D)	0	0

Fig. 4.1 Optimized geometries of benzyl-NCO calculated at the APFD/aug-cc-pVTZ level of theory. In this figure, the numbering system for the carbon atoms is shown in the conformer I geometry. [a]Population distribution calculated using ZPE corrected electronic energies at 298.15 K.

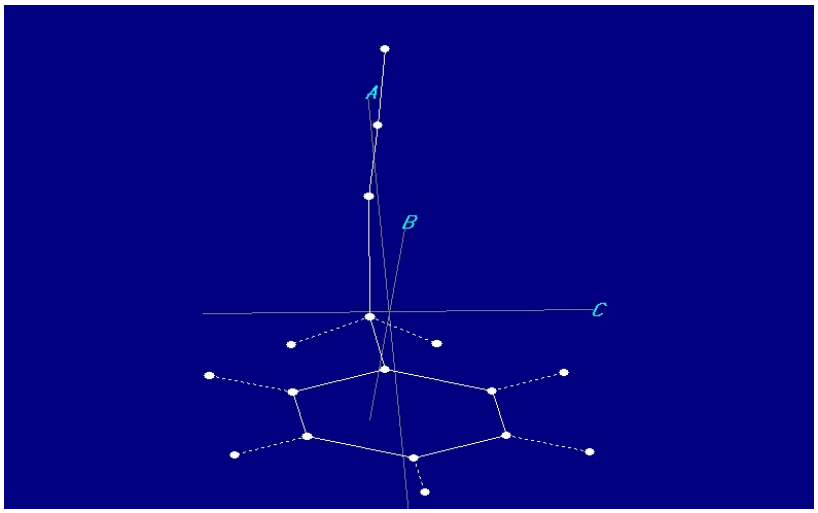

Fig. 4.2 Structure of benzyl-NCO conformer I calculated at the APFD/aug-cc-pVTZ level showing the a, b and c principal inertial axes.

Through Fig. 4.1 and 4.2, it can be seen that the symmetry about the a-rotational axis for conformer I is such that transitions due the $^{13}C_2$ and $^{13}C_6$ isotopic species were found to be equivalent as was the case for $^{13}C_3$ and $^{13}C_5$ and as a result, transitions due to the $^{13}C_2$ and $^{13}C_6$ isotopic species were identified with the $^{13}C_2$ label and the $^{13}C_3$ and $^{13}C_5$ transitions were identified with the $^{13}C_3$ label. A sample of the broadband spectrum from 8000 to 10 800 MHz is given in Fig. 4.3 and shows transitions assigned to the parent species of conformer I as well as the assignment of the 6_{16}-5_{15} transition due to different carbon isotopologues. Additionally, a 0.6 MHz portion of the FTMW spectrum is given in Fig. 4.4 which shows the 10_{19}-9_{18} transition due to the benzyl-NCO conformer I parent species and displays the ^{14}N hyperfine structure for this molecule.

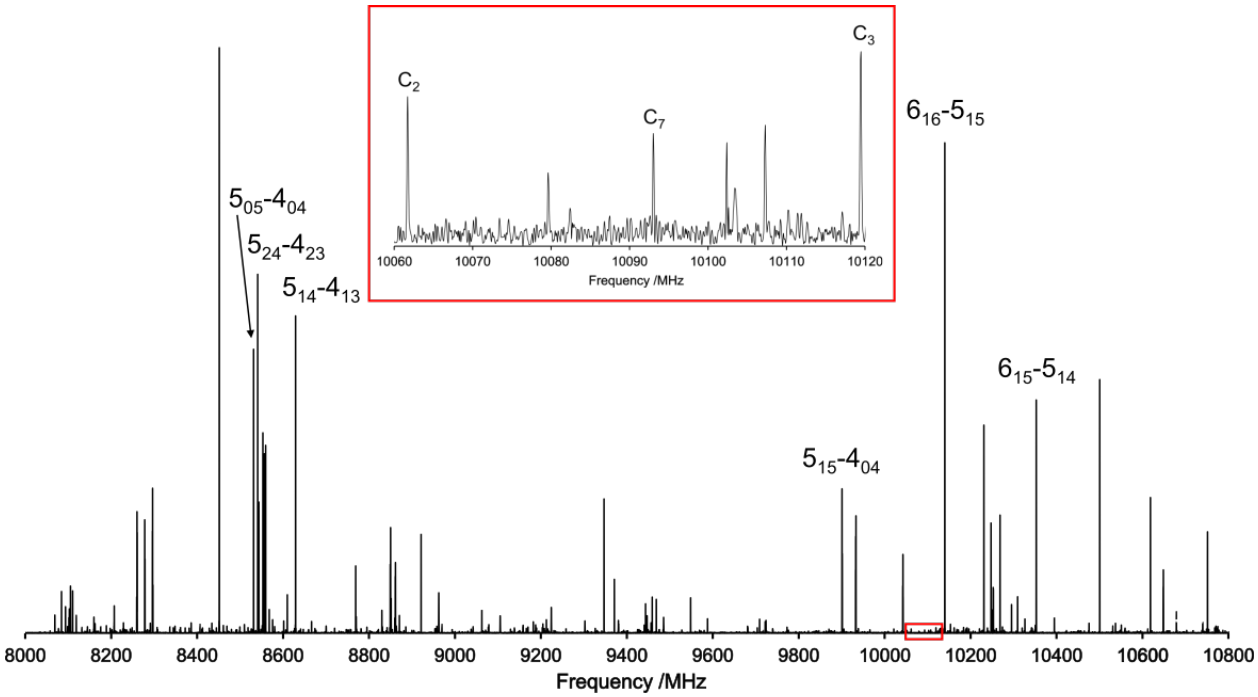

Fig. 4.3 A sample of the benzyl-NCO broadband spectrum from 8000 to 10 800 MHz showing transitions assigned to conformer I. An enhanced portion of the broadband spectrum showing the 6_{16}-5_{15} transition for different ^{13}C isotopologues is highlighted by a red rectangle.

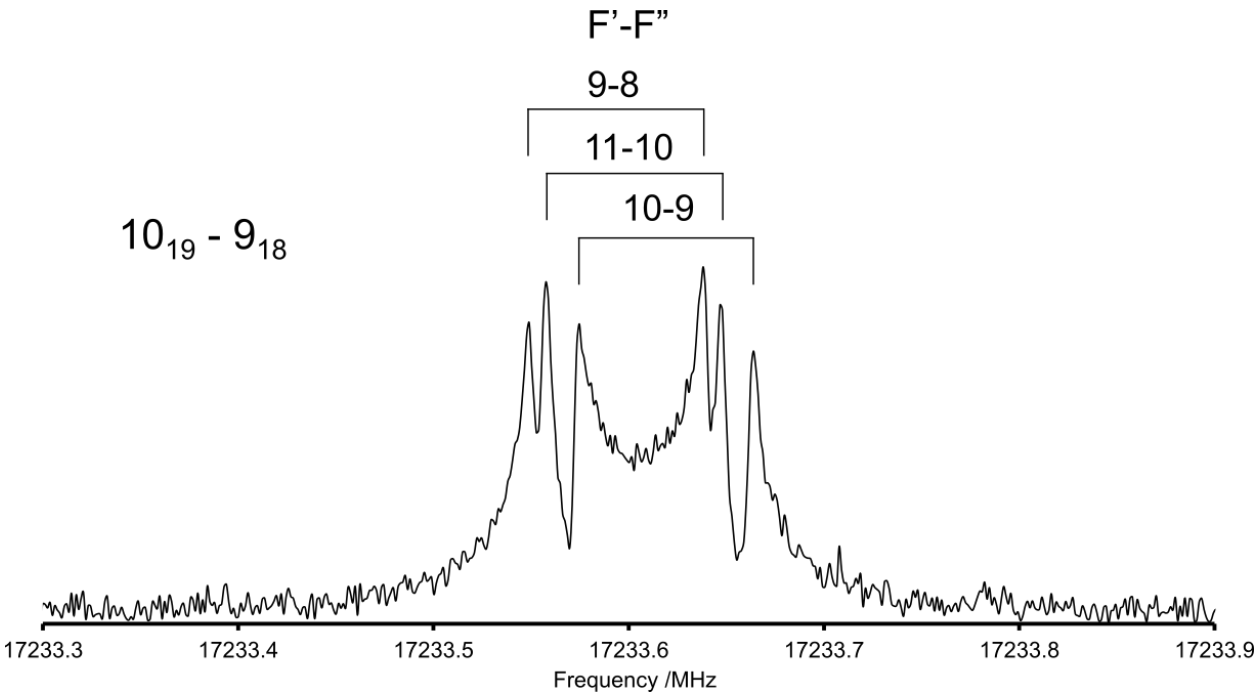

Fig. 4.4 A 0.6 MHz segment of the benzyl-NCO FTMW spectrum showing the 10_{19}-9_{18} rotational transition for benzyl-NCO conformer I (820 cycles). In this figure, the assigned hyperfine structure due to the quadrupolar ^{14}N nucleus can be seen as well as the Doppler splitting caused by the introduction of the molecular beam parallel to the cavity axis.

Rotational transitions were not attributed to the ^{15}N or ^{18}O isotopologues as a result of a combination of the high boiling point of benzyl-NCO (~ 103°C at 33 mm Hg[18]) as well as the low relative abundance of these two minor isotopologues. Transitions due to the benzyl-NCO conformer I parent species and each carbon isotopologue were fit via Pickett's SPFIT program[19] using Watson's S-reduced Hamiltonian in the I^r representation[20] for reasons discussed in chapter 2. The resulting spectroscopic constants for the parent species and unique carbon isotopologues are shown in Table 4.1.

Table 4.1 Rotational, centrifugal distortion and ^{14}N quadrupole coupling constants for the parent species and unique ^{13}C minor isotopologues of benzyl-NCO conformer I as well as those same parameters calculated at the APFD/aug-cc-pVTZ level.

	APFD[a]	Parent	$^{13}C_1$	$^{13}C_2$	$^{13}C_3$	$^{13}C_4$	$^{13}C_7$	$^{13}C_8$
Rotational Constants /MHz								
A	2498.05	2474.5790(6)	2467.920(3)	2455.741(1)	2455.521(1)	2467.465(1)	2446.076(2)	2471.722(2)
B	862.63	872.13616(5)	861.7856(1)	863.7326(1)	868.8391(1)	872.0973(1)	870.6937(2)	863.9571(1)
C	828.97	836.58446(5)	826.2890(1)	830.6220(1)	835.3463(1)	835.7115(1)	831.9423(1)	828.7306(1)
Centrifugal Distortion Constants /kHz								
D_J	0.86	1.1669(1)	1.1250(6)	1.1489(3)	1.1677(4)	1.1632(5)	1.1592(7)	1.1347(6)
D_{JK}	8.23	15.427(2)	14.76(3)	15.420(7)	15.70(1)	15.214(9)	14.54(1)	15.35(1)
D_K	-7.79	[-7.79][b]	[-7.79][b]	[-7.79][b]	[-7.79][b]	[-7.79][b]	[-7.79][b]	[-7.79][b]
d_1	-0.05	-0.0610(2)	-0.0584(7)	-0.0603(5)	-0.0587(6)	-0.0615(6)	-0.0614(8)	-0.0597(8)
d_2	0.25	0.3945(1)	0.379(1)	0.3877(2)	0.3957(3)	0.3932(2)	0.3949(6)	0.3802(2)
^{14}N Quadrupole Coupling Constants /MHz								
1.5 χ_{aa}	-0.10	-0.343(8)	[-0.343][c]	[-0.343][c]	[-0.343][c]	[-0.343][c]	[-0.343][c]	[-0.343][c]
0.25 (χ_{bb}-χ_{cc})	0.75	0.7670(8)	0.772(9)	0.768(1)	0.766(1)	0.770(1)	0.771(2)	0.756(8)
rms /kHz	-	1.1	1.2	0.9	1.1	1.1	1.3	1.1
no. lines[d]	-	130	42	54	54	51	40	40

[a]Calculated using aug-cc-pVTZ basis set. [b]Parameter fixed to calculated value. [c]Paramter fixed to parent value. [d]Number of lines includes hyperfine components.

4.5 Structural Determination

Due to the observation of the parent and carbon minor isotopologue transitions for benzyl-NCO conformer I, an r_0 structure was derived using Kisiel's STRFIT program[21] with the resulting parameters shown in Table 4.2 along with the corresponding r_e structural parameters for benzyl-NCO as well as those of the equivalent benzyl-NCS conformer, both of which were calculated at the APFD/aug-cc-pVTZ level of theory. When deriving the r_0 structure, all parameters related to the hydrogen atoms were fixed to the corresponding r_e structure values.

Table 4.2 r_0 structure for benzyl-NCO conformer I along with the corresponding r_e structure calculated at the APFD/aug-cc-pVTZ level and the r_e structure of benzyl-NCS conformer I calculated at the same level of theory.

	Benzyl-NCO		Benzyl-NCS
	r_e[a]	r_0[b]	r_e[a]
r C_2-C_1	1.389	[1.389]	1.387
r C_3-C_2	1.388	1.400(9)	1.390
r C_4-C_3	1.391	1.398(7)	1.389
r C_5-C_4	1.391	[1.391]	1.392
r C_6-C_5	1.388	[1.388]	1.386
r C_1-C_6	1.389	[1.389]	1.390
r C_7-C_4	1.503	1.507(8)	1.507
r N-C_7	1.445	1.447(4)	1.429
r C_8-N	1.200	[1.200]	1.186
r O/S-C_8	1.169	[1.169]	1.581
∠ C_3-C_2-C_1	120.0	120.4(4)	120.0
∠ C_4-C_3-C_2	120.4	120.1(5)	120.4
∠ C_5-C_4-C_3	119.2	[119.2]	119.4
∠ C_6-C_5-C_4	120.4	121.0(4)	120.3
∠ C_1-C_6-C_5	120.0	[120.0]	120.1
∠ C_2-C_1-C_6	119.9	[119.9]	119.8
∠ C_7-C_4-C_3	120.4	[120.4]	120.5

∠ N-C_7-C_4	113.2	[113.2]	112.8
∠ C_8-N-C_7	136.5	134.4(3)	147.5
∠ O/S-C_8-N	173.9	173.8(6)	176.4
τ C_4-C_3-C_2-C_1	0.0	[0.0]	0.3
τ C_5-C_4-C_3-C_2	0.0	[0.0]	359.7
τ C_6-C_5-C_4-C_3	0.0	[0.0]	0.1
τ C_1-C_6-C_5-C_4	0.0	[0.0]	0.2
τ C_2-C_1-C_6-C_5	0.1	[0.1]	359.8
τ C_3-C_2-C_1-C_6	359.9	[359.9]	359.9
τ C_7-C_4-C_3-C_2	177.7	[177.7]	179.9
τ N-C_7-C_4-C_3	88.9	88.9(1)	117.1
τ C_8-N-C_7-C_4	0.0	[0.0]	26.4
τ O/S-C_8-N-C_7	180.0	[180.0]	177.5

[a]r_e structure calculated at the APFD/aug-cc-pVTZ level. [b]Fit based APFD/aug-cc-pVTZ structure. Brackets indicate parameter fixed to corresponding r_e structure value.

4.6 Discussion

Calculating the benzyl-NCO PES at the APFD/aug-cc-pVTZ level yielded the two minima shown in Fig. 4.1; conformer I which has the NCO group above the phenyl ring and conformer II which has the entire heavy atom backbone in the same plane as the phenyl ring with the NCO group pointed away from the ring. A NCI analysis was done on the lowest energy conformer to determine whether its geometry could be explained by favourable intramolecular interactions between the NCO group and the phenyl ring and the results are shown in Fig. 4.5. As indicated by the red colour and shape of the isosurface, only repulsive interactions within the phenyl ring are found in benzyl-NCO conformer I. This removes the possibility of attractive intramolecular interactions as an explanation of the energetic favourability of benzyl-NCO conformer I over conformer II and thus, the stabilization of conformer I relative to conformer II must be explained by minimizing repulsive effects (either electrostatic or steric) rather than being driven by attractive forces.

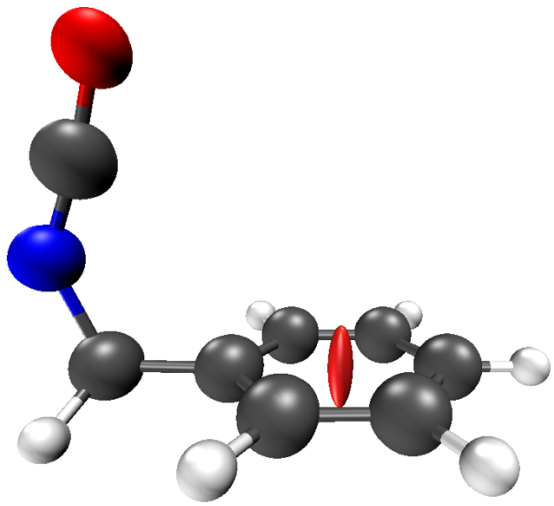

Fig. 4.5 NCI analysis showing the intramolecular interactions of benzyl-NCO conformer I.

In terms of the benzyl-NCO computational benchmarking work, to determine which level of theory most accurately modeled the benzyl-NCO conformational landscape, the spectroscopic constants for conformer I calculated at different levels of theory were compared to the corresponding experimental values to produce Table 4.3. From this table, the results indicate that overall, the constants determined using the APFD method provided the closest agreement with experiment. Furthermore, this table also shows that the experimental distortion constants are not in good agreement with the calculated values from any of the levels of theory selected. Multiple transitions were re-examined in the FTMW spectrum and with no obvious errors in the assignment, the poor agreement of the distortion constants may indicate a failure of the utilized functionals to model the centrifugal distortion effects. A comparison of calculated and experimental quadrupole coupling constants showed reasonable agreement on the value of 0.25 (χ_{bb}-χ_{cc}) while the 1.5 χ_{aa} values were found to not be in as good agreement further highlighting the dispute between the calculated and experimental data. In order to examine whether or not this difference is due to the inability of the selected levels of theory to accurately model the benzyl-NCO hyperfine structure and to attempt to resolve the differences in the distortion constants, the structure of conformer I

can be optimized using more accurate methods such as CCSD(T)[22] and correcting the rotational constants by including vibrational effects however this is beyond the scope of the present work.

Table 4.3 Comparison between experimentally derived spectroscopic constants and those determined at different levels of theory for benzyl-NCO conformer I.

	Experiment	B3LYP	B3LYP-D3(BJ)	wB97XD	APFD
Rotational Constants /MHz					
A	2474.5790(6)	2582.89	2490.86	2512.41	2498.05
B	872.13616(5)	816.33	860.42	858.47	862.63
C	836.58446(5)	782.22	826.32	825.71	828.97
Centrifugal Distortion Constants /kHz					
D_J	1.1669(1)	1.01	0.78	0.83	0.86
D_{JK}	15.427(2)	0.24	6.88	7.28	8.23
D_K	[-7.79][a]	5.71	-6.40	-6.79	-7.79
d_1	-0.0610(2)	0.15	-0.04	-0.04	-0.05
d_2	0.3945(1)	-0.05	0.22	0.23	0.25
^{14}N Quadrupole Coupling Constants /MHz					
1.5 χ_{aa}	-0.343(8)	0.32	-0.07	-0.13	-0.10
0.25 (χ_{bb}-χ_{cc})	0.7670(8)	0.43	0.74	0.73	0.75
rms /kHz	1.1	-	-	-	-
no. lines[b]	130	-	-	-	-

[a]Parameter fixed to value calculated at the APFD/aug-cc-pVTZ level. [b]Number of lines includes hyperfine components. For all methods, Dunning's aug-cc-pVTZ basis set used.

On the benzyl-NCO PES, two conformers were predicted as shown in Fig. 4.1 and yet, as seen in Fig. 4.4, only transitions due to conformer I were assigned even though conformer II is predicted to be ~ 37 % populated at 298.15 K and to have dipole moment components similar to the global minimum. To determine if the absence of conformer II is due to a relaxation to conformer I in the supersonic jet, the transition state was optimized at the AFPD/aug-cc-pVTZ level with frequency calculations and the resulting structure is shown in Fig. 4.6. From this

calculation, the ZPE corrected energy of the transition state was compared to that of conformers I and II to produce Fig. 4.7 where the conformer II→I relaxation barrier was determined to be ~ 0.58 kJ/mol. Furthermore, barriers lower than ~ 4.8 kJ/mol allow for conformer relaxation in a supersonic jet[23] as discussed in chapter 3 and thus, it is likely that conformer II relaxes to conformer I during the jet expansion which would justify why transitions due to conformer II could not be assigned in the rotational spectrum.

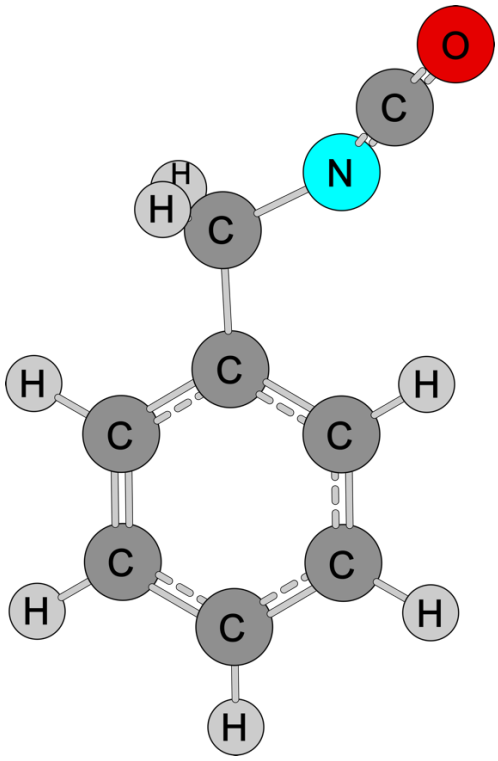

Fig. 4.6 Optimized geometry of the benzyl-NCO transition state for the interconversion of conformer I and conformer II as determined at the APFD/aug-cc-pVTZ level of theory.

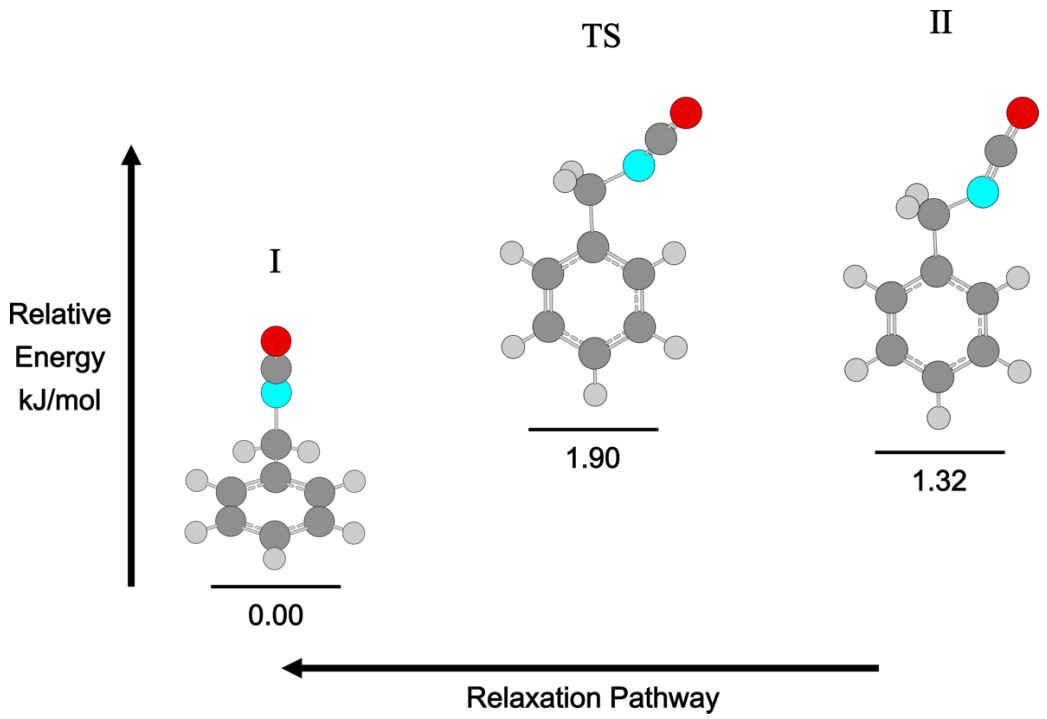

Fig. 4.7 Energy profile for the interconversion of conformers I and II showing the ZPE corrected barrier for benzyl-NCO at 298.15 K. In this figure, the ZPE corrected energies were calculated at the APFD/aug-cc-pVTZ level of theory and the y-axis is not to scale.

Similarly, when modelling the benzyl-NCS PES, two conformers were observed as seen in Fig. 4.8 and when their ZPE corrected energies are combined with that of the transition state (which is shown in Fig. 4.9), the energy diagram in Fig. 4.10 is produced. Fig. 4.10 reveals that the analogous barrier for benzyl-NCS is even lower (~ 0.21 kJ/mol) than its oxygen counterpart thereby predicting that should the rotational spectrum of benzyl-NCS be collected, conformer II would not be observable in a supersonic jet expansion.

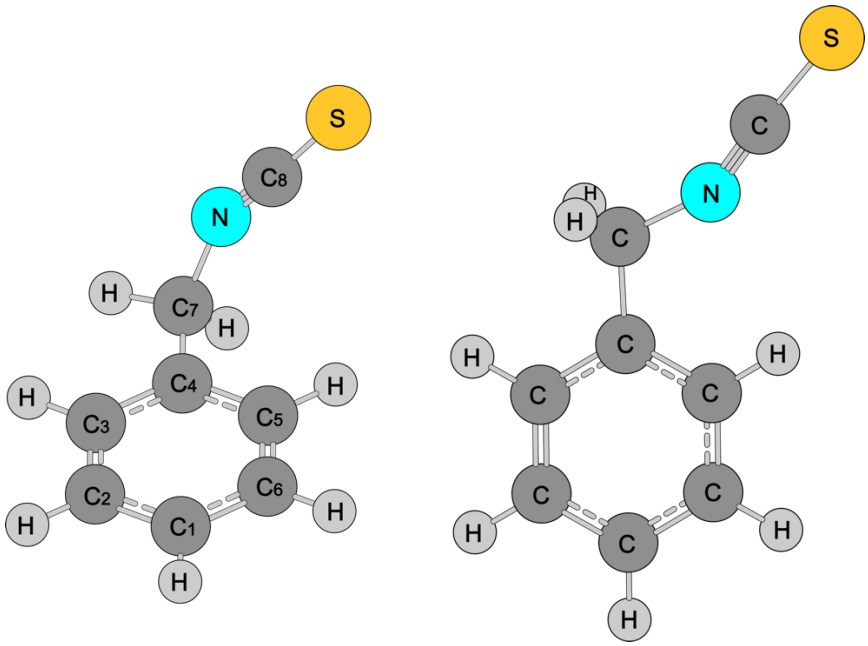

Conformer	I	II
Population (%)[a]	54	46
$\lvert\mu_a\rvert$ (D)	3.0	3.1
$\lvert\mu_b\rvert$ (D)	1.3	1.4
$\lvert\mu_c\rvert$ (D)	0.8	0

Fig. 4.8 Optimized geometries of benzyl-NCS conformers I and II calculated at the APFD/aug-cc-pVTZ level of theory. In this figure, the numbering system for the carbon atoms is shown in the conformer I geometry. [a]Population distribution calculated using ZPE corrected electronic energies at 298.15 K.

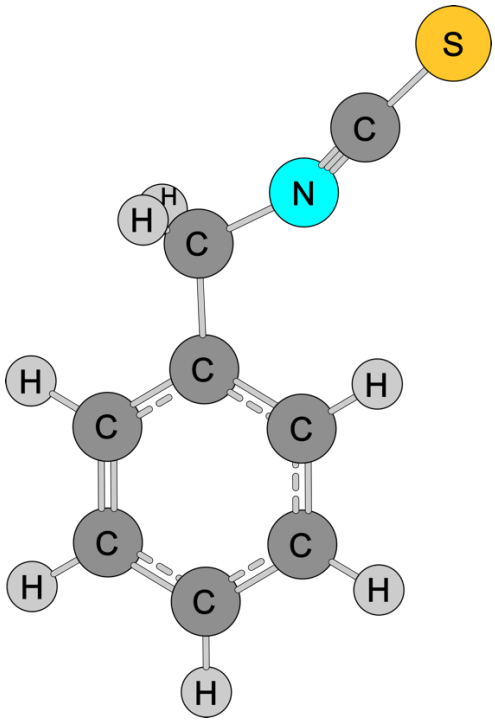

Fig. 4.9 Optimized geometry of the benzyl-NCS transition state for the interconversion of conformers I and II as determined at the APFD/aug-cc-pVTZ level of theory.

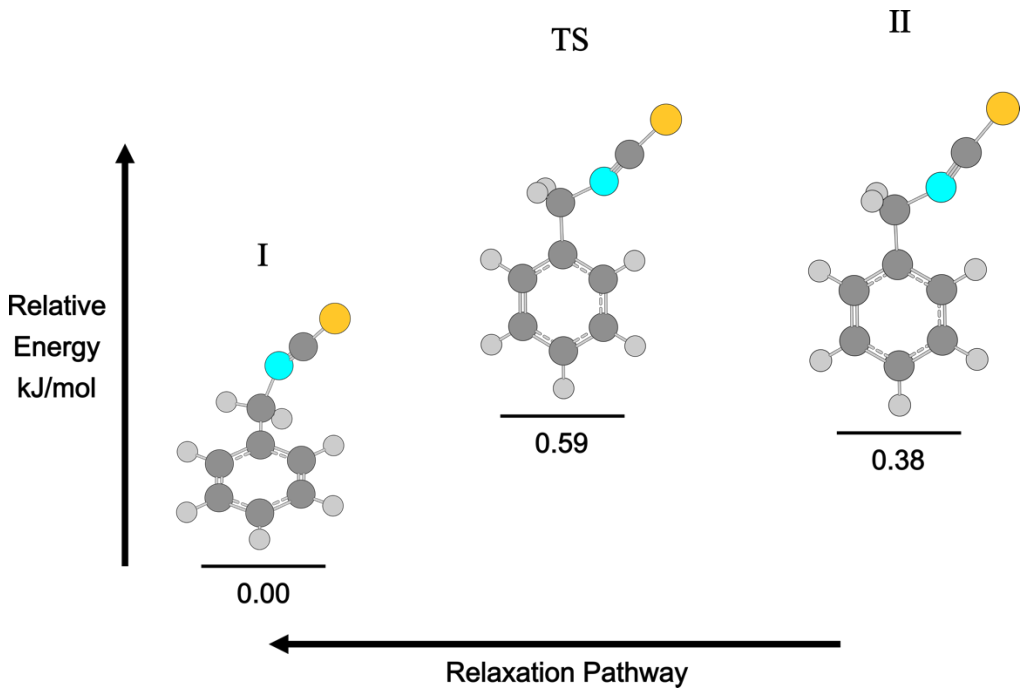

Fig. 4.10 Energy profile for the interconversion of conformers I and II showing the ZPE corrected barrier for benzyl-NCS at 298.15 K. In this figure, the ZPE corrected energies were calculated at the APFD/aug-cc-pVTZ level of theory and the y-axis is not to scale.

To evaluate the change in structure around nitrogen due to a change in the R group, an r_0 structure was derived for benzyl-NCO conformer I using STRFIT with the results shown in Table 4.2 along with the corresponding r_e structural parameters of both benzyl-NCO and it sulfur counterpart. An initial inspection of Table 4.2 indicates that the benzyl-NCO structural fit is of high accuracy as the experimentally fit structural parameters were in agreement with the corresponding r_e values within experimental error aside from the C_8-N-C_7 bond angle which differed by 2.1° and the C_6-C_5-C_4 bond angle which differed by 0.2°. Further proof of the high accuracy of this structural fit comes from a comparison between experimentally derived rotational constants and those calculated by STRFIT as the largest difference was ~ 0.01 %.

Focusing on those structural parameters which involve nitrogen, Table 4.2 shows that the N-C_7 bond length was determined to be 1.447(4) Å which matches the equivalent bond length derived for allyl-NCO conformer I[6] (1.453(22) Å) within experimental error but was found to be ~ 0.043 Å longer than the equivalent bond length from the phenyl-NCO mass dependence ($r^{(1)}_m$) structure.[5] Furthermore, the 134.4° CNC bond angle derived for benzyl-NCO was found to be ~ 3° smaller than the CNC bond angle for allyl-NCO conformer I[6] but only ~ 0.1° smaller than the CNC bond angle of phenyl-NCO[5] when accounting for experimental error thereby providing contradictory evidence as to how the nitrogen electronic environment of benzyl-NCO relates to other isocyanates. However, the r_0 structures of benzyl-NCO and allyl-NCO[6] were compared to the $r^{(1)}_m$ structure of phenyl-NCO[5] which may affect the results and so, to form a conclusion as to which nitrogen electronic environment is most similar to that of benzyl-NCO, the r_e structural parameters around nitrogen were compared for the three isocyanates and the results are shown in Table 4.4. From this table, it can be seen that the results above are confirmed as the benzyl-NCO CN bond lengths are most similar to those of its allyl counterpart while the CNC bond angle in benzyl-NCO is predicted to be identical to that of phenyl-NCO meaning that no initial conclusion can be drawn on the relationship between the nitrogen electronic environment of the benzyl group and other isocyanates based on the geometric parameters alone.

Table 4.4 Analogous r_e structural parameters around nitrogen for benzyl, allyl and phenyl-NCO. In this table, the numbering of the carbon atoms is in reference to the benzyl-NCO numbering scheme.

	Benzyl-NCO[a]	Allyl-NCO[b,c]	Phenyl-NCO[d,e]
r N-C_7	1.445	1.438	1.399
r C_8-N	1.200	1.197	1.214
∠ C_8-N-C_7	136.5	138.8	136.5

[a]r_e structure calculated at the APFD/aug-cc-pVTZ level. [b]Structure determined at the B3LYP-D3(BJ)/cc-pVQZ level. [c]Ref. 6. [d]r_e structure calculated at the MP2/aug-cc-pVTZ level. [e]Ref.5.

As the structural comparisons above provided no conclusive evidence as to which nitrogen electronic environment was most similar to that of benzyl-NCO, an NBO analysis was conducted on benzyl-NCO with the results then compared to the allyl-NCO analysis from chapter 3 as well as a previous analysis done on phenyl-NCO[5] in order to address this question. For benzyl-NCO conformer I, the hybridization of the nitrogen bonding molecular orbital along the C_8-N and N-C_7 bonds was determined to be ~ $sp^{1.5}$ and ~ $sp^{1.9}$, respectively. A comparison of the NBO results found this bonding character to be most similar to the analogous ~ $sp^{1.5}$ and ~ $sp^{1.8}$ orbitals, respectively in allyl-NCO which suggests the electronic environment around nitrogen for the benzyl group is most similar to that of the allyl group. This leads to the conclusion that the nitrogen electronic environment is heavily influenced by the side chain structure immediately around the nitrogen atom and is largely unaffected by more distant changes in the side chain structure. These results were in agreement with the initial predictions that the benzyl-NCO nitrogen electronic environment would be most similar to its allyl counterpart since both the allyl and benzyl side chains both contain a methylene carbon and because a portion of the benzyl side chain structure is nearly identical to that of the allyl group.

For the benzyl group, the comparison of the benzyl-NCS r_e structure to that of its oxygen counterpart in Table 4.2 predicts that chalcogen substitution has no impact on the side chain structure as previously indicated for the allyl group[6]. When considering the structural parameters around the nitrogen atom, Table 4.2 indicates that chalcogen substitution in the benzyl r_e structures results in N-C_7 and C_8-N bond length decreases of 0.016 Å and 0.014 Å, respectively in addition to an 11° increased in the CNC bond angle. A comparison with the allyl[6] and phenyl[5] group r_e structures reveals that the changes in bond length are more closely aligned with the effects observed for the allyl group where decreases of 0.015 Å and 0.013 Å, respectively were observed for the equivalent bonds while the change in the CNC bond angle for the benzyl group is most similar to the predicted ~ 10.1° increase for the phenyl group.[5] These results seem to indicate that the CNC angle may be strongly affected by the bulk of the R group rather than the linking group. To clarify this, the NBO results discussed above for benzyl-NCO were compared to a NBO analysis done on its sulfur counterpart where, for the nitrogen atom, the bonding molecular obrital along the N-C_7 bond changed from a ~ $sp^{1.9}$ to a ~ $sp^{1.1}$ shape as a result of oxygen to sulfur substitution while the C_8-N bond changed from a ~ $sp^{1.5}$ to a ~ sp orbital. These results are most closely aligned with the predicted variations in nitrogen hybridization for the allyl group where in the equivalent N-C_7 bond, a change from a ~ $sp^{1.8}$ to a ~ $sp^{1.1}$ hybridized orbital is calculated and for the equivalent C_8-N bond, a change from a ~ $sp^{1.5}$ to a ~ sp hybridized orbital is predicted. This provides additional evidence that small changes in side chain structure do have an impact on the nitrogen electronic environment as long as these structural changes are within the immediate vicinity of the nitrogen atom but it also suggests that other effects like steric bulk cannot be discounted.

References

(1) Hocking, W. H.; Gerry, M. C. L. The Microwave Spectrum of Cyanogen Isocyanate (NCNCO). *J. Mol. Spectrosc.* **1976**, *59* (3), 338–354.

(2) King, M. A.; Kroto, H. W.; Landsberg, B. M. Microwave Spectrum of the Quasilinear Molecule, Cyanogen Isothiocyanate (NCNCS). *J. Mol. Spectrosc.* **1985**, *113* (1), 1–20.

(3) Ham, N. S.; Willis, J. B. The Vibrational Spectra of Organic Isothiocyanates. *Spectrochim. Acta.* **1960**, *16* (3), 279–301.

(4) Fisher Scientific. Benzyl isothiocyanate, 98%, ACROS Organics https://www.fishersci.com/shop/products/benzyl-isothiocyanate-98-acros-organics-3/AC402130050 (accessed Jan 29, 2020).

(5) Sun, W.; Silva, W. G. D. P.; van Wijngaarden, J. Rotational Spectra and Structures of Phenyl Isocyanate and Phenyl Isothiocyanate. *J. Phys. Chem. A.* **2019**, *123* (12), 2351–2360.

(6) Sun, W.; Sogeke, O. P.; Silva, W. G. D. P.; van Wijngaarden, J. Dispersion-Driven Conformational Preference in the Gas Phase: Microwave Spectroscopic and Theoretical Study of Allyl Isocyanate. *J. Chem. Phys.* **2019**, *151* (19), 194304.

(7) Becke, A. D. Density-functional Thermochemistry. III. The Role of Exact Exchange. *J. Chem. Phys.* **1993**, *98* (7), 5648–5652.

(8) Stephens, P. J.; Devlin, F. J.; Chabalowski, C. F.; Frisch, M. J. Ab Initio Calculation of Vibrational Absorption and Circular Dichroism Spectra Using Density Functional Force Fields. *J. Phys. Chem.* **1994**, *98* (45), 11623–11627.

(9) Grimme, S.; Antony, J.; Ehrlich, S.; Krieg, H. A Consistent and Accurate Ab Initio Parametrization of Density Functional Dispersion Correction (DFT-D) for the 94

Elements H-Pu. *J. Chem. Phys.* **2010**, *132* (15), 154104.

(10) Grimme, S.; Ehrlich, S.; Goerigk, L. Multidimensionality of Delocalization Indices and Nucleus Independent Chemical Shifts in Polycyclic Aromatic Hydrocarbons. *J. Comput. Chem.* **2011**, *32* (7), 1456–1465.

(11) Dunning, T. H. Gaussian Basis Sets for Use in Correlated Molecular Calculations. V. Core-valence Basis Sets for Boron through Neon. *J. Chem. Phys.* **1989**, *90* (2), 1007–1023.

(12) Kendall, R. A.; Dunning, T. H.; Harrison, R. J. Electron Affinities of the First-row Atoms Revisited. Systematic Basis Sets and Wave Functions. *J. Chem. Phys.* **1992**, *96* (9), 6796–6806.

(13) Woon, D. E.; Dunning, T. H. Gaussian Basis Sets for Use in Correlated Molecular Calculations. III. The Atoms Aluminum through Argon. *J. Chem. Phys.* **1993**, *98* (2), 1358–1371.

(14) Austin, A.; Petersson, G. A.; Frisch, M. J.; Dobek, F. J.; Scalmani, G.; Throssell, K. A Density Functional with Spherical Atom Dispersion Terms. *J. Chem. Theory. Comput.* **2012**, *8* (12), 4989–5007.

(15) Chai, J.-D.; Head-Gordon, M. Systematic Optimization of Long-Range Corrected Hybrid Density Functionals. *J. Chem. Phys.* **2008**, *128* (8), 084106.

(16) Chai, J.-D.; Head-Gordon, M. Long-Range Corrected Hybrid Density Functionals with Damped Atom–Atom Dispersion Corrections. *Phys. Chem. Chem. Phys.* **2008**, *10* (44), 6615–6620.

(17) Grimme, S. Semiempirical GGA-Type Density Functional Constructed with a Long-Range Dispersion Correction. *J. Comput. Chem.* **2006**, *27* (15), 1787–1799.

(18) Fisher Scientific. Benzyl isocyanate, 99+%, ACROS Organics https://www.fishersci.com/shop/products/benzyl-isocyanate-99-acros-organics-2/AC210760050 (accessed Apr 2, 2020).

(19) Pickett, H. M. The Fitting and Prediction of Vibration-Rotation Spectra with Spin Interactions. *J. Mol. Spectrosc.* **1991**, *148* (2), 371–377.

(20) Watson, J. K. G. *Vibration Spectra and Structure*; Durig, J., Ed.; Elsevier: Amsterdam, 1977.

(21) Kisiel, Z. PROSPE - Programs for ROtational SPEctroscopy http://www.ifpan.edu.pl/~kisiel/prospe.htm (accessed Nov 8, 2019).

(22) Gauss, J.; Stanton, J. F. Analytic CCSD(T) Second Derivatives. *Chem. Phys. Lett.* **1997**, *276* (1–2), 70–77.

(23) Ruoff, R. S.; Klots, T. D.; Emilsson, T.; Gutowsky, H. S. Relaxation of Conformers and Isomers in Seeded Supersonic Jets of Inert Gases. *J. Chem. Phys.* **1990**, *93* (5), 3142–3150.

Chapter 5. Conclusions and Future Work

The work done in this thesis focused on a microwave and computational study of allyl-NCS and benzyl-NCO in addition to a computational study of benzyl-NCS as examples of prototypical isocyanate and isothiocyanate species in order to probe how the nitrogen electronic environment is impacted by changes in the side chain structure in addition to chalcogen substitution. The rotational spectra were obtained using a broadband cp-FTMW spectrometer and a narrowband FTMW spectrometer, both of which are custom-built instruments in the van Wijngaarden lab.

In the allyl-NCS study, constructing a 3D PES at the B3LYP-D3(BJ)/cc-pVTZ level revealed the same two conformers that had been previously identified[1–3] in addition to the lowest energy conformer which has been reported for the first time. The presence of this geometry in the allyl-NCS conformational landscape was confirmed by the assignment of transitions due to both the parent species as well as the heavy atom minor isotopologues which also allowed for a derivation of the r_0 structure. A comparison of the r_0 structure with allyl-NCO[4] revealed that oxygen to sulfur substitution causes a ~ 15° increase in the CNC angle which was found to be most similar to the ~ 14° increase observed for the cyano side chain[5,6] and demonstrates that there is not a simple relationship between the R group and the electronic environment at nitrogen.

Additionally, in this thesis, the microwave spectrum of benzyl-NCO was recorded for the first time where transitions were assigned to the global minimum conformer and the corresponding ^{13}C isotopologues. Furthermore, the benzyl-NCO computational benchmark showed that when the parent transitions were fit, the resulting set of spectroscopic constants were in closest agreement with calculations at the APFD/aug-cc-pVTZ level. To evaluate the impact of the side chain structure on the nitrogen electronic environment, the benzyl-NCO r_e structure was compared to its

allyl[4] and phenyl[7] counterparts where no conclusion could be drawn from the calculated geometries alone. This was resolved by conducting an NBO analysis on the optimized benzyl-NCO geometry where it was revealed that the nitrogen bonding molecular orbitals are more similar to allyl-NCO[4] than phenyl-NCO[7] which suggests that only the portion of the side chain structure near the nitrogen atom impacts the nitrogen electronic environment.

Since the gas phase microwave spectrum of benzyl-NCS could not be collected due to the high boiling point[8], instead, the r_e structure of benzyl-NCS conformer I was calculated at the APFD/aug-cc-pVTZ level and compared to the corresponding benzyl-NCO r_e structure. Such a comparison revealed that oxygen to sulfur substitution is predicted to cause a ~ 0.015 Å decrease in CN bond lengths and a ~ 11° increase in the CNC angle but a comparison of these results to the allyl[4] and phenyl[7] groups again provided unclear evidence as to how the change in the nitrogen electronic environment for the benzyl group relates to other side chains. Conducting an NBO analysis on benzyl-NCS and comparing the results to benzyl-NCO revealed that the predicted changes in the hybridization of the nitrogen bonding molecular orbitals are most similar to the allyl group which provided additional evidence that the overall nature of the R group does not have a significant influence on the nitrogen atom. However, the allyl-NCS study showed that structural changes due to terminal chalcogen substitution for the allyl group were most similar to the cyano group[5,6] which does not have structural similarities around the nitrogen atom. The results of this thesis therefore demonstrate that changes in the nitrogen electronic environment occur due to a balance of effects caused by R group and chalcogen substitution.

The results of this thesis work has a number of applications. For example, similar to the laboratory studies mentioned in section 1.1, the laboratory rotational spectra of allyl-NCS and benzyl-NCO can act as a reference when examining the rotational spectrum of different portions

of interstellar space in order to determine if either allyl-NCS or benzyl-NCO are present in the region of space being explored which would help to explain the chemistry of the interstellar medium. Additionally, the results of this thesis show how different levels of theory produce different conformational landscapes and by using the experimental results from the allyl-NCS and benzyl-NCO studies, computational methods can be better parameterized so that they provide results more closely aligned with the experimental data for these molecules and other similar compounds. More generally, if the structural changes due to side chain or chalcogen substitution are known, the enhancement or reduction in strength of intermolecular interactions can be determined which has numerous applications including in the pharmaceutical industry. For example, five hydrogen bonds occur between a bacterial cell and the antibiotic vanomycin which prevents the building up of the bacterial cell wall when it binds to a bacterial cell.[9] In this case, if one or more of the vanomycin oxygen atoms involved in hydrogen bonding is replaced with sulfur, then this will change the molecular structure as well as the distance of these groups relative to their hydrogen bond partners.[9] This, in combination with the reduced electronegativity of the sulfur atom compared to the oxygen atom will lead to a reduction in the strength of the hydrogen bonds meaning that the vanomycin molecule will not be as tightly bound which will reduce its effectiveness as an antibiotic.[9] Therefore, by knowing the impact of the changes due to chalcogen substitution then the structure of a potential drug could be altered in order to change the properties to suit a particular objective.

The work done in this thesis can be extended by collecting and analyzing the benzyl-NCS rotational spectrum. As mentioned in this thesis, the boiling point of benzyl-NCS is high enough such that a gas phase microwave spectrum could not be collected. However, the van Wijngaarden group is currently working on a heated nozzle which should provide the additional energy required

to put benzyl-NCS into the gas phase such that the gas phase microwave spectrum could be recorded. Repeating the benzyl-NCO procedure for its sulfur counterpart, a structural derivation could be done for the benzyl-NCS global minimum which would provide an experimental change in the nitrogen electronic environment due to chalcogen substitution for the benzyl group. This change can then be compared to other R groups in order to determine experimentally how the different side chain structures influence the electronic environment around nitrogen. Furthermore, if heated nozzle testing is successful, then the rotational spectrum of benzyl-NCO could be recollected using this nozzle setup so that transitions can be assigned due to the ^{15}N and ^{18}O isotopologues which will allow for the fitting of additional structural parameters and should provide a more precise molecular structure.

The results of this thesis can also be extended by conducting a microwave study on phenethyl isocyanate ($C_6H_5C_2H_4$-NCO) and phenethyl isothiocyanate ($C_6H_5C_2H_4$-NCS) whose rotational spectra have not been previously collected. By studying these molecules and then comparing the results to those of the phenyl and benzyl groups, the role that the proximity of the nitrogen atom to the phenyl ring has on the nitrogen electronic environment can be determined. However, there are additional complications when doing such a study as there are three variable dihedral angles in the phenethyl group which means that the process described in this thesis to model the conformational landscape of allyl-NCS and both benzyl molecules will need to be extended. Furthermore, the high boiling points of both phenethyl isocyanate (210°C[10]) and phenethyl isothiocyanate (139-140°C at 11 mmHg[11]) indicate that it will be difficult to put either molecule into the gas phase so such a study should not be done until heated nozzle testing has been completed.

References

(1) Maiti, S.; Jaman, A. I.; Nandi, R. N. Microwave Spectrum of Allyl Isothiocyanate: Gauche Conformer. *J. Mol. Spectrosc.* **1994**, *165* (1), 168–172.

(2) Jaman, A. I. Centrifugal Distortion Analysis of the Microwave Spectrum of Allyl Isothiocyanate (C-Gauche Conformer). *PRAMANA-J. Phys.* **1999**, *53* (5), 857–862.

(3) Glaser, R.; Hillebrand, R.; Wycoff, W.; Camasta, C.; Gates, K. S. Near-Silence of Isothiocyanate Carbon in 13C NMR Spectra: A Case Study of Allyl Isothiocyanate. *J. Org. Chem.* **2015**, *80* (9), 4360–4369.

(4) Sun, W.; Sogeke, O. P.; Silva, W. G. D. P.; van Wijngaarden, J. Dispersion-Driven Conformational Preference in the Gas Phase: Microwave Spectroscopic and Theoretical Study of Allyl Isocyanate. *J. Chem. Phys.* **2019**, *151* (19), 194304.

(5) Hocking, W. H.; Gerry, M. C. L. The Microwave Spectrum of Cyanogen Isocyanate (NCNCO). *J. Mol. Spectrosc.* **1976**, *59* (3), 338–354.

(6) King, M. A.; Kroto, H. W.; Landsberg, B. M. Microwave Spectrum of the Quasilinear Molecule, Cyanogen Isothiocyanate (NCNCS). *J. Mol. Spectrosc.* **1985**, *113* (1), 1–20.

(7) Sun, W.; Silva, W. G. D. P.; van Wijngaarden, J. Rotational Spectra and Structures of Phenyl Isocyanate and Phenyl Isothiocyanate. *J. Phys. Chem. A.* **2019**, *123* (12), 2351–2360.

(8) Fisher Scientific. Benzyl isothiocyanate, 98%, ACROS Organics https://www.fishersci.com/shop/products/benzyl-isothiocyanate-98-acros-organics-3/AC402130050 (accessed Jan 29, 2020).

(9) Schaeffer, L. Chapter 14 - The Role of Functional Groups in Drug–Receptor Interactions. In *The Practice of Medicinal Chemistry*; Elsevier, 2008; pp 359–378.

(10) Sigma-Aldrich. Phenethyl isocyanate 98% https://www.sigmaaldrich.com/catalog/product/aldrich/456179?lang=en&region=CA (accessed Apr 25, 2020).

(11) Sigma-Aldrich. Phenethyl isothiocyanate 99% https://www.sigmaaldrich.com/catalog/product/aldrich/253731?lang=en&region=CA (accessed Apr 25, 2020).